Research paper

On the effect of design and fabrication parameters on mechanical performance of 3D printed PLA scaffolds

R. Baptista[a,d,*] ricardo.baptista@estsetubal.ips.pt, M. Guedes[a,e], M.F.C. Pereira[b], A. Maurício[b], H. Carrelo[c], T. Cidade[c]

[a]CDP2T, Departamento de Engenharia Mecânica, Escola Superior de Tecnologia de Setúbal, Instituto Politécnico de Setúbal, 2910-761, Setúbal, Portugal

[b]CERENA, DECivil, Instituto Superior Técnico, Universidade de Lisboa, Av. Rovisco Pais, 1, 1049-001, Lisboa, Portugal

[c]Cenimat/I3N, Departamento de Ciência dos Materiais, Faculdade de Ciências e Tecnologia, FCT, Universidade Nova de Lisboa, 2829-516, Caparica, Portugal

[d]IDMEC, Instituto Superior Técnico, Universidade de Lisboa, Av. Rovisco Pais, 1049-001, Lisboa, Portugal

[e]CeFEMA, Instituto Superior Técnico, Universidade de Lisboa, Av. Rovisco Pais, 1049-001, Lisboa, Portugal

*Corresponding author. IDMEC, Instituto Superior Técnico, Universidade de Lisboa, Av. Rovisco Pais, 1049-001, Lisboa, Portugal.

Abstract

Tissue engineering is responsible for developing biological substitutes that restore, maintain or improve tissue function. A solution to achieve this is to implant scaffolds on the affected tissue. These support structures will be responsible for cell protection, oxygenation and nutrition, while supporting mechanical loads during the regeneration process. They should also be biodegradable in order to be gradually replaced by healthy tissue. From the available scaffolds manufacturing techniques, fused filament fabrication has been used recently. This technique does not use organic solvents and has the ability to produce complex geometries. In this paper the influence of manufacturing parameters was assessed. Different temperatures, extrusion speeds, filament offset distances and layer thicknesses were tested and their effect analyzed regarding scaffold morphology and mechanical properties. By decreasing the filament offset distance, three different scaffolds porosities were obtained, increasing the mechanical properties. Combining higher printing temperatures with slow extrusion speeds and low layer thickness, a maximum yield stress of 28 MPa and apparent compressive modulus of 942 MPa were obtained. With these preferred parameters, two different manufacturing schemes and geometries were tested. While using a double layer printing scheme one obtains an average of 70%

increase in mechanical properties, using a staggered configuration can decrease mechanical properties up to 84%.

Keywords: 3D printing; Bone replacement; Scaffolds; Porosity; Mechanical behavior

1 Introduction

Structural function is the main attribute of the hard tissues in the human skeleton. As a dynamic tissue, bone is in a constant process of remodeling and repair, adapting to the mechanical demands of everyday life. However, bone tissue may suffer trauma, disease or infection, requiring medical regeneration, filling or replacement [1]. More and more often the bone healing response is clinically stimulated through bone grafts or substitute materials, with bone being the second most common transplant worldwide (after blood), with more than four million actions performed annually [1]. To overcome the limitations associated with conventional bone grafts (allo, xeno and autografts), research in Bone Tissue Engineering (BTE) is directed to the creation of alternatives. In this context, the development of porous three-dimensional scaffolds, incorporating osteoblasts and growth factors to support bone regeneration, has become a key engineering area [1].

Scaffold structures mimic the bone microenvironment, allowing the development of living tissue constructions that are structural, functional and mechanically comparable to natural bone [1]. Scaffold are seeded *in vitro* with activated cells and then implanted *in vivo* at the damaged site. They gradually disintegrate and are absorbed into the body, as cells of new biological tissue proliferate through the porous structure [2]. Control of scaffold parameters is essential to guarantee the therapeutic efficacy of the implant, with three main factors to consider: composition, structure and mechanical properties [2,3]. An ideal scaffold consists of biodegradable and biocompatible material (including its degradation products), of suitable composition to provide bioactive environment in which cells attach and proliferate [1]. Both polymeric materials and bioactive ceramics have been used in order to achieve these goals, but lately the use of composite materials is also on the rise [4]. Polylactic acid (PLA), polycaprolactone (PCL), polyether ether ketone (PEEK) or poly (glycolic acid) (PGA) are examples of polymeric materials, while hydroxyapatite (HA) and tricalcium phosphate (TCP) have been used as bioactive ceramics. The macroscale scaffold architecture defines the geometry of the device, designed according to patient and organ specificities, while structure at the microscale reflects the required porosity parameters, which should be projected according to the cells in the tissue to be regenerated [2,5]. Bone tissue regeneration in particular requires high pore fraction (60–90%) to allow cell migration into the structure and to accommodate sufficient cell mass for tissue repair and vascularization, nutrient diffusion and waste excretion [1,2]. Porosity must include macropores in the 100–350 μm range and micropores below 20 μm [6,7]; pore interconnectivity above 50 μm is required to allow cell migration, which is also affected by pore shape and tortuosity [2,7]. The smaller the pore size, the larger the scaffold's surface area, increasing the availability of structural sites for interaction with cells. Scaffolds must also present structural stability similar to the tissue in which it will be implanted [1], while mechanical performance and porosity vary inversely [1,3]. Localized higher porosity (with macropores above 1 mm) might also be used with beneficial results, without affecting scaffold's mechanical properties. Egan et al. have usefully implemented central voids in lattice scaffolds, improving oxygenation and nutrient transport, with almost no impact on scaffold's compression stiffness [8]. Mechanical properties must ensure that the structure may suffer elastic deformation before being implanted without permanent damage, has sufficient strength for handling during sterilization, and provides support when applied *in vivo*, allowing the mechanical use of the new tissues in real environment [2]. The most relevant mechanical properties of scaffold include rigidity, compressive strength and fatigue strength; ideally compressive strength should match that of cortical bone (100–230 MPa),

and Young's modulus of 7–30 GPa [1]. Mechanoregulatory effects are also critical for influencing bone tissue growth and cell differentiation *in vivo*: if forces transferred under physiological conditions are not replicated in the scaffold, the stimulus received by cells may cause them to move away from their osteogenic lineage towards undesirable morphology [1].

To this end, BTE has developed scaffolds using a variety of manufacturing processes and biomaterials, with numerous successful products. However, several scientific and technological challenges remain unmet [1]. Choosing between acellular and cell loaded scaffolds, requiring cell collection and inducing morbidity risk. Generating sufficient scaffold vascularization with enough penetration to ensure cell viability and achieving the desired control over scaffold degradation, without affecting scaffold mechanical properties or inducing inflammatory responses. Tailoring scaffolds mechanical behavior to meet individual necessities, while scaling up scaffold biofabrication, are just a few of these challenges [1,3]. In this context, the current paper approach the need to better adapt scaffolds' mechanical performance to the anatomical loading conditions of individual bone defects, to reduce the occurrence of failure [1]. Achieving satisfactory mechanical performance requires well-applied replication of a set of properties including stiffness, compressive strength and fatigue strength [1], while maintaining an adequate porosity and interconnected pore structure. This work approaches these issues through forming by additive manufacturing (AM), a most promising processing philosophy due to the greater control, precision and repeatability over the architecture, morphology and anisotropy of designed geometries [1,5,9]. In fact, layer-on-layer deposition ensures more precise control over the size, shape and interconnectivity of the macro and micropore structure [10]. Among AM, *fused filament fabrication* (FFF) has been established as a most suitable technology for processing synthetic polymer scaffolds [5,9]. Several studies have previously reported successful *in vitro* use of biocompatible scaffolds resulting from FFF manufacturing of PLA [3,11–13]. Using FFF allows for a biocompatible polymer like PLA in a filament form to be heated, fused, extruded through a nozzle and deposited in a predefined pattern. It is then possible to create from simple to complex scaffolds designs, controlling overall porosity, porous dimensions and connectivity [1]. Without the need for using solvents and other chemical products, this manufacturing technique can be used to print polymer and living cells composites with no toxicity risk, when using a polymer with a low melting temperature [14].

Among the most common synthetic biodegradable polymers in medical applications, polylactic acids (PLAs) are one of the most promising, due to their relatively strong mechanical properties (elastic modulus between 3 and 4 GPa, tensile strength between 50 and 70 MPa) [15,16]. PLAs are aliphatic polyesters, with $(C_3H_4O_2)_n$ backbone and typically low molecular weight (Fig. 1). The abbreviation is taken to represent either poly (lactic acid) (if the material is obtained by step growth polymerization of lactic acid) or polylactide, when obtained by ring-opening polymerization of cyclic lactide) [17–19]. The pure stereo-regular forms of lactic acid are L-lactic acid and D-lactic acid; their polymerization respectively yields poly (L-lactic acid) (PLLA) and poly (D-lactic acid) (PDLA); polymerization of mixtures produces amorphous poly (D,L-lactic acid) (PDLLA) [17–20]. PLA can be either amorphous or semicrystalline (up to 40% crystalline max) depending on its stereochemical architecture and thermal history [21]: PLAs containing more than 93% L-lactic acid can crystallize; yet, if presenting a high molecular weight or if it contains less than 93% L-units, it is usually amorphous [21]. In the biomedical field, the use of PLA has been approved by regulatory agencies in many countries to manufacture various bone implants, including screws and fixation devices [1,15,22]. Amorphous PDLLA is typically used for controlled drug release, while semicrystalline PLLA is selected for applications where higher mechanical and thermomechanical properties are required [16]. PLAs degrade chemically, leading to the formation of low-molar mass polyester fragments, carbon dioxide (CO_2) and water (H_2O) [20]. The human body can reabsorb these products with minimal reaction of the tissues [20]. PLLA is a more slowly degrading polymer than PDLA [20]:

high molar mass PLLA can take from two to five and half years for total resorption *in vivo*; because of its amorphous character, poly (D,L-lactic acid) is hydrolyzed and loses its chain length within 1–2 months and completely loses its mass within 12–16 months [20]. FFF processing makes use of commercial PLA filament. The distribution of repeating units, average molecular weight, degree of crystallinity and glass transition temperature can differ very much in the purchased material, depending on the synthesis route, feed and heating program [19,23]. Purposeful or unintended changes in one or more of these factors cause changes in material bulk characteristics, including mechanical properties, water uptake, and degradation, which in turn will cause a change in cellular reaction to the material after implantation [17].

alt-text: Fig. 1

Fig. 1

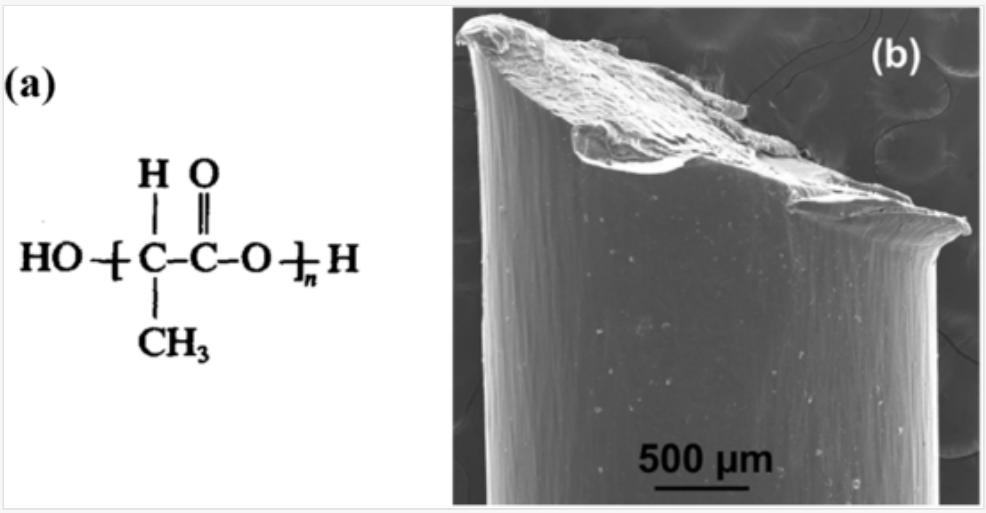

PLA. (a) Polylactic acids structural formula showing the ester group contained within the $CH_3CHC(=O)O$ repeating unit, while alcohol (-OH) and carboxylic acid (-COOH) are the end groups of PLA macromolecules [24]. (b) Sample of the used commercial filament (knife cut).

In this context, this work studies the effect of FFF processing parameters (temperature, speed, orientation, layer thickness) upon a PLA commercial filament, aiming to establish preferred processing parameters rendering structural scaffolds able to mimic the mechanical, morphological and biochemical stimuli to which cells are exposed, improving osteogenesis.

2 Experimental

2.1 Materials

Commercial PLA (Fig. 1a) spooled filament with ∅ 1.75 mm from BQ/Spain (Fig. 1b) was used in the manufacture of all scaffolds. Table 1 shows characteristics of the used filament according to the producer.

alt-text: Table 1

Table 1

The table layout displayed in this section is not how it will appear in the final version. The representation below is solely purposed for providing corrections to the table. To preview the actual presentation of the table, please view the Proof.

Properties of the used PLA filament, according to producer.

PLA (%)	Density (g/cm^3)	T_m (°C)	T_g (°C)	$T_{printing}$ (°C)
100	1.24	145–160	56–64	200–220

T_m: melting temperature; T_g: glass transition temperature; $T_{printing}$: recommended range of printing temperatures.

2.2 PLA characterization

PLA material as-supplied and after FFF processing was characterized by rheological and thermal analysis, scanning electron microscopy (§ 2.4.1), and Raman spectroscopy.

2.2.1 Differential Scanning Calorimetry

Differential Scanning Calorimetry (DSC) was carried out (TA Instruments, Q200) to evaluate the physical transformations taking place and the degree of crystallinity of the PLA polymer with increasing processing temperature. As-supplied samples were tested; samples removed from scaffolds after AM at 200 °C and 220 °C were also tested, to evaluate the effect of thermal history applied during polymer synthesis or processing upon polymer properties [25]. Tests were carried out up to 250 °C, at 10 °C/min heating rate and under nitrogen gas flow (20 ml/min). At least three tests were carried out for each material (approx. 10 mg) to ensure reproducibility. The degree of crystallinity (X_c) (*i.e.*, the percentage of crystalline content in the polymer before thermal analysis) was calculated using Eq. (1) [21,25,26].

$$X_C = 100 \times \frac{\Delta H_m - \Delta H_{cc}}{\Delta H_m^0} \quad (1)$$

where ΔH_{m-} and ΔH_{cc} are respectively the enthalpy of melting and the enthalpy of cold crystallization (which takes place during the measurement); ΔH_m^0 is the enthalpy of melting for a pure PLA crystal of infinite size (93.7 J/g) [27].

2.2.2 Rheology

The viscosity curve of PLA was determined using a Bohlin Gemini HR^{NANO} rotational rheometer. The measurements were performed under a constant temperature of 200 and 220 °C and the measuring system used was cone and plate (1°, 25 mm). Before starting the measurements, the samples were subjected to a pre-shear stage of 10 s^{-1} applied during 60 s followed by an equilibrium time (the time elapsed after stopping the pre-shear and starting the measurements) of 120 s.

The viscosity was measured as a function of the shear rate, which was applied in the range 10–1000 s^{-1}. At least three replicas were considered.

2.2.3 Raman spectroscopy

Identification of the functional groups of PLA as-supplied and after AM and their characterization regarding shape, position and intensity was carried out using Raman spectroscopy (HR Evolution, Horiba Jobin-Yvon). Raman spectra were collected using 532 nm laser, 100× objective, 5 accumulations and 10 s acquisition. All plots were collected in the 200–3200 cm^{-1} spectral range. Daily calibration of the relative line position was

carried out using as reference the 520 cm^{-1} phonon mode from silicon. The software FITYK 0.9.8 [28] was used for background removal and peak fitting, which was carried out with Lorentzian function [29].

2.3 Scaffolds design and manufacturing

Scaffolds were first designed as 12.7 × 12.7 × 25.4 mm blocks (complying with dimensions in ASTM-695 specification) and modeled in Onshape (https://www.onshape.com/) CAD software. Each block was imported to Cura (https://ultimaker.com/software/ultimaker-cura) slicing software and transformed into a scaffold, using no top or bottom layers and no side walls. Offset distance between filaments was set to 1333, 800 and 571 μm, corresponding to 30, 50 and 70% infill respectively. Filaments were layered in a rectangular 0°/90° infill pattern (*Ortho*, Fig. 2a), resulting in 70, 50 and 30% porosity scaffolds with 100% pore interconnectivity. Printing speed of 30 mm/s and 45 mm/s, printing temperature of 200 °C and 220 °C (corresponding to the maximum and minimum printing temperatures recommended by the PLA supplier, Table 1), and layer thickness of 200 μm and 300 μm were tested. A total of 8 different manufacturing parameters combinations were produced for each scaffold porosity, resulting in a total of 24 *Ortho* configurations to be tested (Table 2).

alt-text: Fig. 2

Fig. 2

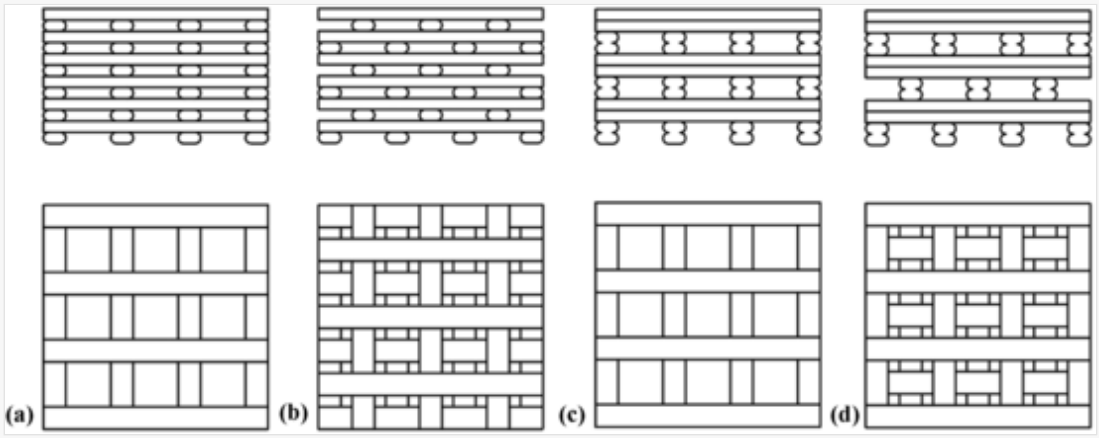

Front and top views of a) single layer, b) single layer staggered, c) double layer and d) double layer staggered orthogonal scaffolds.

alt-text: Table 2

Table 2

The table layout displayed in this section is not how it will appear in the final version. The representation below is solely purposed for providing corrections to the table. To preview the actual presentation of the table, please view the Proof.

Tested FFF printing parameters and manufactured specimens.

Temperature (ºC)	Speed (mm/s)	Infill (%)	Layer thickness (μm)	Design			
				Ortho	Displ	2xOrtho	2xDispl
200	45	30	200	S132			

			300	S133			
		50	200	S152			
			300	S153			
		70	200	S172			
			300	–			
	30	30	200	S232			
			300	S233			
		50	200	S252			
			300	S253			
		70	200	S272			
			300	S273			
220	45	30	200	S332			
			300	S333			
		50	200	S352			
			300	S353			
		70	200	S372			
			300	S373			
	30	30	150			2S4315	
			200	S432	ST432	2S432	2ST432
			300	S433	ST433	2S433	2ST433
		50	150			2S4515	
			200	S452	ST452	2S452	2ST452
			300	S453	ST453	2S453	2ST453
		70	150			2S4715	
			200	S472	ST472	2S472	2ST472
			300	S473	ST473	2S473	2ST473

The *Ortho* samples were submitted to compression mechanical test (§ 2.4.3), and the processing parameters rendering the best mechanical performance were selected to produce additional designs (Table 2). On this second phase, the original manufacturing *gcode* files were manually configured. The first two layers designed by Cura were copied along the height direction and offsetted in the xy plane. The correct layer height coordinate and the necessary material amount to be extruded, are easily calculated using and Excel spreadsheet and exported as a gcode file. Manually configured *gcodes* have many advantages [3]: material deposition pattern can be customized, including layer thickness, printing speed and temperature, and filament offset distance. This enabled more complex designs to be created, and three different configurations were then designed. Offsetting one layer

allowed to obtain a staggered configuration (*Displ*, Fig. 2b), in which sequential layers do not share the same support points, therefore introducing structural bending and reducing overall structural rigidity. By repeating the same layer, a double layer configuration was achieved (*2xOrtho*, Fig. 2c) and *2xDispl*, Fig. 2d), increasing the dimension of the scaffold lateral pores. A special 150 μm layer thickness *2xOrtho* series of scaffolds was printed in order to isolate the scaffold's lateral pore dimension effect, when compared against 300 μm *Ortho* series.

All specimens were printed in a Blocks Zero (Blocktec) 3D Printer. Each scaffold layer was printed in a single motion, by printing parallel filaments in opposite directions. This process maintains filament characteristics in each layer but has the disadvantage of producing scaffolds with partially closed pores on the side walls. For each configuration three samples were produced (n = 3), for reproducibility assessment throughout all further tests.

2.4 Scaffolds characterization

2.4.1 Scanning electron microscopy

The morphology, porosity and defect features of as-supplied filament and of produced PLA scaffolds were analyzed by scanning electron microscopy (SEM) (Hitachi S2400). Samples for SEM observation were previously coated with Au–Pd alloy to assure adequate electrical conductivity. Dimensions of as-supplied filament, scaffold pore design size and scaffold filament diameter and overall compliance to projected dimensions were carried out by image analysis using the ImageJ freeware (https://imagej.nih.gov/ij/); at least 20 random positions were measured in each sample for reproducibility assessment.

2.4.2 Micro-CT analysis

The analysis of the morphological and internal structure of the scaffolds was made using an X-ray micro-CT scanner (Skyscan 1172 MicroCT, Kontich, Belgium)). X-ray digital radiographs were recorded at different angles during step-wise rotation between 0 and 180° around the vertical axis, with 0.5° rotation step. Samples were scanned at a voltage of 100 kV with current intensity of 100 μA. The pixel resolution was set at 18.09 μm and two sequential acquisitions were performed for each scaffold. Acquired image data were qualitatively and quantitatively interpreted using 3D tomographic reconstruction NRecon®, visualization (CTVox®) and calculation (CTAn®) softwares.

2.4.3 Mechanical testing

Scaffolds were tested under monotonic compression, accordingly to ASTM-695 standard, using an electromechanical test machine (TS300, Impact Test Equipment). Design and manufacturing parameters influence on scaffold mechanical behavior was analyzed, determining specimen apparent compressive yield stress σ. The specimen compressive modulus E was also determined, considering that specimen strain ε is obtain dividing specimen height variation Δh by the specimen initial height h_0.

$$E = \frac{\sigma}{\varepsilon} \tag{2}$$

Each specimen series (n = 3) was tested using a constant 1 mm/min speed, using a 50 kN load cell. In order to identify possible significant statistical differences between different manufacturing parameters and scaffolds geometries, Kruskal-Wallis non-parametric test for small samples was used, with $\alpha = 0.05$.

3 Results

3.1 Effect of processing temperature upon PLA polymer

FFF requires processing temperature above the polymer melting point, for the chains to move relative to each other, allowing polymer to flow. Melt flow is dominated by viscosity and influenced by many other polymer characteristics (nature, grade and additives) and flow conditions (melt temperature, flow rate, channel size, and melt pressure) [30], and it is determinant for materials' extrusion and printability [31]. Under these circumstances, it is useful to assess the relationship between FFF temperature and dynamic properties of the material, through rheological, measurements [32]. This is particularly important in the case of PLA, given the unique nature of its rheology: besides presenting strain hardening extensional behavior, its chemical stability can be adversely affected above the melting temperature, where both chain hydrolysis and pyrolysis become important [32]. Fig. 3 shows viscosity evolution of the used commercial PLA with increasing shear rate, at 200 °C (Figs. 3a) and 220 °C (Fig. 3b).

alt-text: Fig. 3

Fig. 3

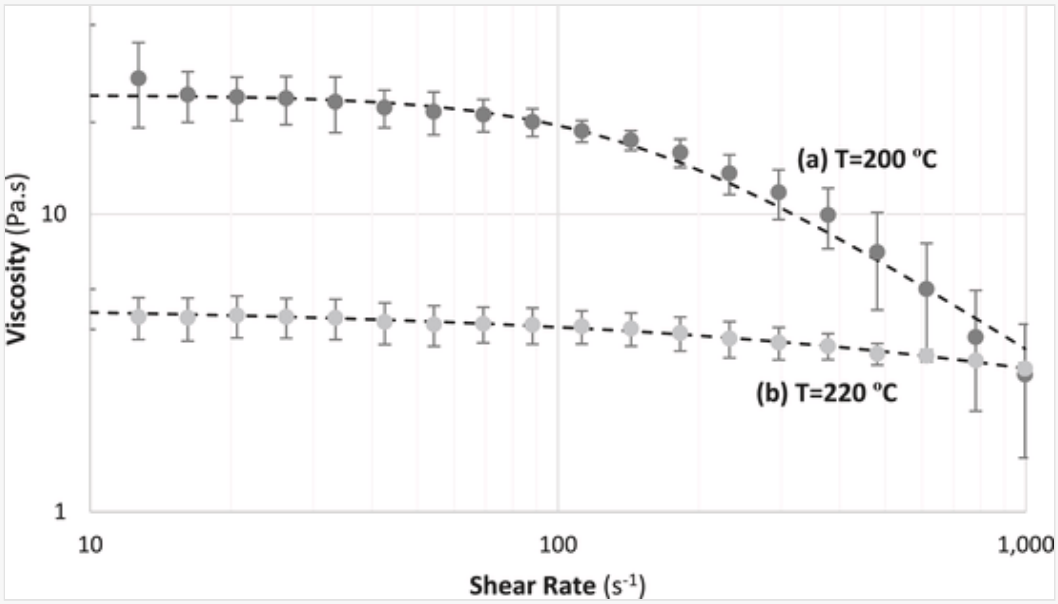

Viscosity vs shear rate log curves for BQ PLA melts at (a) 200 °C and (b) 220 °C (which correspond to the tested printing temperatures), fitted using the Bird-Carreau-Yasuda model [33].

Both temperatures are sufficiently above the melting temperature (please refer to Fig. 3) for the polymer to behave as a liquid with measurable viscosity. As expected [32,34], PLA shows shear-thinning rheological behavior at both tested temperatures, corresponding to viscosity decrease with increasing shear rate (and shear strain). The value of zero-shear viscosity η_0 as the shear rate approaches zero is approx. 28.6 Pa s at 200 °C and 4.6 Pa s at 220 °C. Both curves present a lengthy lower Newtonian region, respectively up to $\dot{\gamma}_c$ = 100 s^{-1} and $\dot{\gamma}_c$ = 223 s^{-1}, followed by the shear-thinning zone. Within the tested shear rate range, the upper Newtonian region was not reached; also viscosity values are always lower at 220 °C than at 200 °C. The melt viscosity performance described in Fig. 3 is expected to be considerably dependent on the weight average molar mass of PLA at the tested temperatures [35]: the higher the molar mass, the higher the chain length and its degree of entanglement, leading to decreased chain flexibility and higher melt viscosity for low and intermediate shear rate range [34,35]. The quite abrupter slope change at the end of the lower Newtonian region of the 200 °C curve

appears to confirm more extensive entanglements between PLA molecules, which correspond to strong couplings that act in a localized manner, contributing to increased material elasticity (similarly to cross-links) [34]. At this lower temperature, viscosity increases rapidly and polymer melt is expected to display a more pronounced elastic recovery from any deformation [34] than at 220 °C.

The crystallinity, glass transition, cold crystallization and melting of PLA were assessed by DSC (Fig. 4a) Samples removed from FFF specimens printed at 200 °C (Fig. 4b) and 220 °C (Fig. 4c) were also submitted to thermal analysis. Table 3 summarizes the corresponding transformation onset and peak maximum, and the percentage crystallinity (X_c) in the materials (Eq. (1)).

alt-text: Fig. 4

Fig. 4

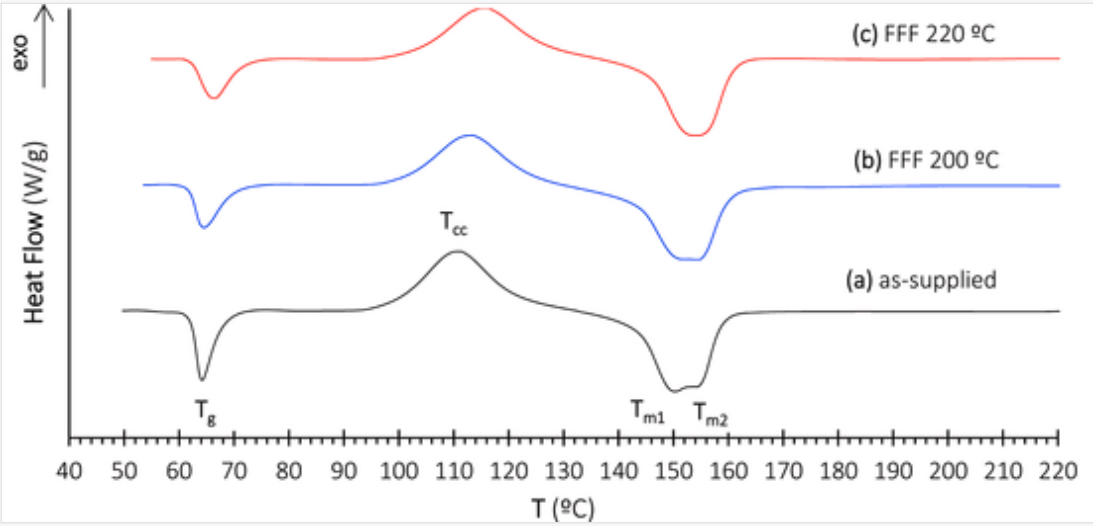

DSC plots on heating up to 240 °C: (a) as-supplied PLA; (b) PLA after FFF at 200 °C followed by air cooling; and (c) after FFF at 220 °C followed by air cooling.

alt-text: Table 3

Table 3

The table layout displayed in this section is not how it will appear in the final version. The representation below is solely purposed for providing corrections to the table. To preview the actual presentation of the table, please view the Proof.

Transformation temperatures and crystallinity vs polymer thermal history.

Filament	Glass transition		Cold crystallization			Melting			
	T_g (ºC)	T_{peak} (ºC)	T_{cc} (ºC)	T_{peak} (ºC)	X_{cc} (%)	onset (ºC)	Tm_1 (ºC)	Tm_2 (ºC)	X_c (%)
As-supplied	62	65	99	110	74.6	144	150	155	3.1
After FFF at 200 ºC	62	65	100	114	69.9	150	151	155	6.9
After FFF at 220	62	67	102	117	65.2	146	–	155	30.9

°C									

All obtained DSC heating plots show endothermic peaks corresponding to glass transition and to crystal melting, and one exothermic peak corresponding to cold crystallization. In every case, melting is finished below 160 °C, well below both tested FFF temperatures. The as-supplied commercial PLA material is expected to have been formed to filament shape by melt extrusion, the most important technique for PLA forming in many conversion processes of continuous profiles [36]. To ensure that all the crystalline phases in PLA are melted and to achieve an optimal melt viscosity for processing, the extruder heater is usually set at 200–210 °C [36]. The commercial PLA material tested already carries a previous thermal history. The onset of glass transition for as-supplied PLA filament (Fig. 4a, Table 3) takes place at 62 °C, in good agreement with reported values [17,19–21]. Cold crystallization starts at approx. 99 °C and corresponds to an extent of crystallization of 74.6%. Cold crystallization is typical of polymers prone to crystallize but that have previously been cooled quickly enough to avoid chain rearrangement [21]. This indicates that filament cooling rate in the course of its extrusion process is fast enough for the resulting PLA filament to remain mainly amorphous [25]. However, although during DSC molecular mobility is severely restricted below Tg, small crystallites are allowed to form in the polymer above that temperature, and PLA's ability to rearrange manifests. The cold crystallization process is finished below 122 °C, and melting takes place afterwards, with onset at 144 °C. Two melting peaks appear to overlap, with peak maxima at 150 and 155 °C. The presence of two peaks is expected to result from a change in crystal morphology: T_{m1} corresponds to melting of spherulites (formed at lower crystallization temperature), while T_{m2} corresponds to melting of hexagonal crystals (formed at higher crystallization temperature) [21,25]. The calculated intrinsic as-supplied polymer crystallinity (after subtracting cold crystallization) is only 3.1%. The DSC plot of the material after withstanding FFF at 200 °C (Fig. 5b, Table 3) is quite similar, although a two-fold increase in polymer crystallinity (6.9%) and a lower percentage of crystallites formed on cold crystallization (69.9%, corresponding to a 6.3% decrease) result. The similarity is expected to arise from the fact that both systems were (expectedly) cooled from approx. the same temperature, rendering similar rearrangement by the end of the corresponding cooling step. However, after withstanding FFF at 220 °C, striking differences arise on PLA melting behavior (Fig. 5c, Table 3). Glass transition and cold crystallization present less 12.6% and 6.7% cold crystallization when compared to as-supplied material and to material FFF at 200 °C, respectively. Also, only one melting peak arises (with peak maximum at 155 °C) and overall melting enthalpy (corresponding to the area below the melting peak in the corresponding DSC plot) is quite high, as well as intrinsic crystallinity (30.9%, corresponding to almost a ten-fold increase compared to as-supplied material). The higher crystallinity is expected to result from the overall lower melt viscosity at 220 °C (Fig. 3), rendering higher chain mobility [21,26]. Chain mobility is also improved by the lower chain length at 220 °C. Finally, the supercooling range is much more extended than when cooling starts at 200 °C, providing increased time for crystal nucleation and growth [21], and allowing full transformation of spherulites into the higher temperature hexagonal-shaped crystals. The presence of a single polymorph is thus expected to correspond to a single melting peak in Fig. 5c.

alt-text: Fig. 5

Fig. 5

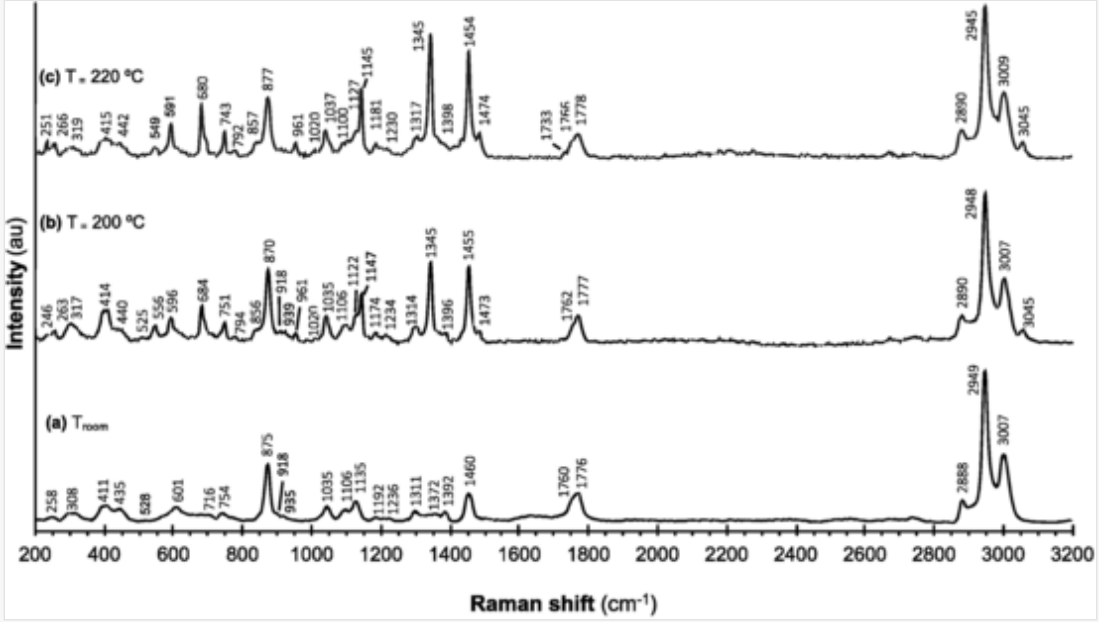

Raman plots of the used PLA in the 200 to 3200 cm^{-1} spectral range: (a) room temperature, and after heating at (b) 200 °C and (c) 220 °C.

Filament as-supplied, and material after FFF at 200 and 220 °C was also submitted to Raman spectroscopy (Fig. 5), since changes in the Raman spectra of lactic acids can be correlated with their polymerization degree [24], crystallinity level [18], and stereo configuration [37]. Besides the repeating unit, PLA (Fig. 1) contains an alcohol (-OH) and a carboxylic acid (-COOH) end group. Changes in the crystallinity degree and average chain size can be followed by analyzing the position and/or intensity of Raman peaks characteristic of the vibrations modes of the repeat unit (C=O, COC, and *C*–C), in comparison to end groups modes [24]. In as supplied PLA (Fig. 5a) the characteristic peak for C=O stretching appeared as a broad asymmetric band around 1776 cm^{-1}. The fact that this band is not sharp and well defined indicates that the material is mainly amorphous [18,19], although the splitting shoulder (1760 cm^{-1}) suggests some degree of crystallinity. This is confirmed by the presence of bands at 308, 411, 528 and 935 cm^{-1}, as well as by bands at 1392 and 1311 cm^{-1}: although these bands are very weak in the obtained spectra, they are indicative of some degree of crystallinity among the disordered structure [18,19]. The strong band at around 875 cm^{-1} (ester *C*–COO stretching) has also been assigned to semicrystalline PLA [38]. The asymmetry of the C=O band (1776 cm^{-1}) appears to increase with increasing processing temperature (Fig. 5b and c), suggesting decreasing perturbation of the helical chain structure of PLA.

The sharp peak splitting at 1345 cm^{-1} is expected to be due to crystallinity [19], in good agreement with the evolution in crystalline contents determined by DSC (Table 3). This new peak increases intensity and narrows from 200 to 220 °C, characteristic of a higher crystallinity degree. The variation of the maximum intensity ratio of the *C*–COO peak around 875 cm^{-1} and the CH_3 asymmetric bending around 1460 cm^{-1} has been related to the degradation of the PLA chain [24]. The value of the $I_{875}/_{1745}$ intensity ratio is 1.98 in as-supplied filament, decreasing to 0.91 and to 0.61 in PLA extruded at 200 °C and at 220 °C, respectively. It is thus expected that increasing degradation is taking place with increasing AM temperature, with separation of water soluble oligomers within the polymer [23,37]. This is supported by presence of very weak bands around 1240 cm^{-1} (CO stretching of the acid end group coupled to OH bending of the end alcohol group), 1106 cm^{-1} (CO stretching of the end alcohol group), and 856 cm^{-1} (*C*–COOH stretching of the end alcohol group) [24]: the

appearance of bands associated to the end groups is related with a decreasing average number of units in the polymer chain, with the number of end groups proportionally raising as the total chain length decreases [24]. The absence of a band around 1745 cm^{-1} allows to establish that the poly (D,L-lactide) stereo complex is not present [38], in good agreement with the high achievable crystallinity in the system at 220 °C.

Overall, results from rheologic, thermal and spectroscopic analysis suggest that the used commercial PLA is a low molecular weight polymer containing only L-units, mainly with amorphous character and slow crystallization ability. Processing at 200 °C slightly increases the crystalline extent and introduces crystal polymorphs. Increasing FFF temperature to 220 °C noticeably promotes crystallization on cooling, while it also leads to polymer degradation with chain length decrease, with implications in the selection of processing parameters.

3.2 Effect of processing parameters upon PLA printability

PLA printability at both tested temperatures can be estimated from its rheological properties together with manufacturing parameters. The printing pressure ΔP necessary to achieve the desired melt volume flow rate (Q) through a nozzle of radius (R) and length (L) at a specified flow rate can be calculated using (Eq. (3)) [31].

$$\Delta P = \frac{8\eta Q L}{\pi R^4} \tag{3}$$

The influence of temperature and shear rate $\dot{\gamma}$ upon steady state shear viscosity η of a shear-thinning polymer melt can be fitted with the Bird-Carreau-Yasuda model (Eq. (4)) [33]:

$$\frac{\eta - \eta_\infty}{\eta_0 - \eta_\infty} = \left[1 + |\lambda\dot{\gamma}|^a\right]^{\frac{n-1}{a}} \tag{4}$$

where η_0 is the zero shear rate viscosity, η_∞ the infinite shear rate viscosity value (negligible), λ the relaxation time, n the power law index and a a constant (originally considered by Bird-Carreau equal to 2). Material flow Q and shear rate $\dot{\gamma}$ can be calculated respectively from Eq. (5) and the Rabinowitsch equation (Eq. (6)) [31].

$$Q = v \cdot t \cdot d \tag{5}$$

$$\dot{\gamma} = \frac{4Q}{\pi R^3} \tag{6}$$

where v is the printing speed, t the layer thickness and d the nozzle exit diameter. Table 4 summarizes the calculated flow, shear rate and printing pressure, considering a filament diameter of 1.75 mm and a nozzle exit diameter of 400 μm.

alt-text: Table 4

Table 4

The table layout displayed in this section is not how it will appear in the final version. The representation below is solely purposed for providing corrections to the table. To preview the actual presentation of the table, please view the Proof.

Calculated shear rate, material viscosity and necessary printing pressure at nozzle entrance and exit, considering different processing temperature, printing speed and designed layer thickness.

	Layer Thickness (μm)		**200**	**200**	**300**	**300**
	Printing Speed (mm/s)		**30**	**45**	**30**	**45**
	Material flow (mm^3/s)		**2.4**	**3.6**		**5.4**
	Entrance	$\dot{\gamma}$ **(1/s)**	**4.56**	**6.84**		**10.26**
Printing Temperature (ºC)	Exit	$\dot{\gamma}$ (1/s)	381.97	572.96		859.44
200	Entrance	η (Pa.s)	25.09	25.06		25.00
	Exit	η (Pa.s)	8.58	5.97		4.07
	Entrance	ΔP (Pa)	2877	4′311		6′451
	Exit	ΔP (Pa)	16′388	17′108		17′495
	Total	ΔP (Pa)	19′265	21′418		23′945
220	Entrance	η (Pa.s)	4.75	4.72		4.67
	Exit	η (Pa.s)	3.60	3.38		3.13
	Entrance	ΔP (Pa)	545	811		1′205
	Exit	ΔP (Pa)	6′875	9′669		13′441
	Total	ΔP (Pa)	7′420	10′480		14′645

Fig. 3 shows two different material behaviors. When printing at a lower temperature (200 °C), PLA filament changes behavior from Newtonian to power-law, as material flows from the nozzle entrance to its exit. Table 4 shows shear rate increasing from 4.56 1/s to 10.26 1/s on the nozzle entrance, as layer thickness and printing speed increases. This corresponds to a Newtonian material behavior resulting in a higher material viscosity, but due to the higher nozzle diameter, the resulting necessary pressure to keep material flow is very low (maximum of 6′451 Pa). When exiting the nozzle, shear rate can increase up to 859.44 1/s, setting the material on the power-law region, reducing viscosity to 5.00 Pa s and increasing the necessary flow pressure to 17′495 Pa. Therefore, when using demanding printing conditions (high printing speeds and layer thickness) at low temperatures, the printer may lack the ability to push the filament, leading to nozzle clogging. And even if the printer is able to develop the necessary pressure, the filament may buckle also leading to nozzle clogging [31]. This was verified on our experiment, as it was not possible to print scaffolds with 70% infill, with a 45 mm/s printing speed and 300 μm layer thickness at 200 °C (Table 1). Print at higher temperatures (220 °C), Table 4 and Fig. 3 shows that PLA filament will behave as a quasi-Newtonian fluid, with a viscosity ranging from 4.75 to 3.13 Pa s, reducing the total amount of pressure necessary to print the material, from 23′945 Pa (200 °C) to

14′645 Pa (220 °C). A minimum 39% reduction, when printing with the most demanding conditions, will lead to higher quality printed scaffolds.

3.3 Selection of preferred printing parameters

Successful FFF manufacture requires the combination of a set of fundamental conditions [31]: the material must adequately flow through a given diameter nozzle at a specified flow rate; the extruded material must hold the desired shape and must be dimensionally stable during transition to the final solid state at room temperature; the extruded structure must be able to perform under the imposed mechanical requirements. In this context, the *Ortho* geometry scaffolds configurated in the Cura software (Table 2) were used to assess the parameters combinations rendering higher printability.

Fig. 6 summarizes the geometrical features of produced *Ortho* scaffolds. The measured printed filament width varies considerably depending on processing parameters. Overall, FFF at 200 °C (Fig. 6a) appears to result in higher scattering of filament width values, ranging from to 389 ± 19 μm (30 mm/s, 30% infill, 300 μm tailored thickness, Fig. 7a) to 313 ± 39 μm (45 mm/s, infill 50%, 300 μm, Fig. 7b), while it was not even possible to print the 70% infill scaffold (45 mm/s, 300 μm) due to lack of material extrusion. Regardless of printing speed, geometric compliance at 200 °C appears to decrease with infill when the tailored thickness is 300 μm, yet it increases with increasing infill when tailored thickness is 200 μm. Increasing the printing speed to 45 mm/s and the layer thickness to 300 μm, increases the material flow up to 5.4 mm^3/s. Although the material behavior changes from Newtonian to power-law (Table 4), decreasing viscosity to 5.00 Pa s, nozzle geometry leads to an overall pressure increase to 23′945 Pa. As a result, the printer was not able to extrude the necessary amount of material. As the infill parameter is increased from 30% to 70%, more material must be extruded through the nozzle, and since the printer lacks this ability, filament width will decrease, eventually leading to nozzle clogging [31]. On its turn, filament width resulting from FFF at 220 °C (Fig. 6b) ranged from approx. 393 μm (samples printed at 30 mm/s and 300 μm tailored thickness, regardless of the infill, Fig. 7d–f) to 341 ± 53 μm (45 mm/s, 30%, 200 μm, Fig. 7c). In every case attained width values are lower than the used nozzle diameter (400 μm), with a deviation between −2.7% and −21.7% for FFF at 200 °C, and between −1.7% and −14.7% for FFF at 220 °C. Regardless of printing speed, geometric compliance at 220 °C again increases with increasing infill when tailored thickness is 200 μm, yet it is approx. constant when the tailored thickness is 300 μm. Fig. 3 shows a reduced material viscosity when printing at 220 °C, leading to overall reduced printing pressures (Table 4). The printer is therefore able to extrude the necessary amount of material, and the final filament width will depend on the remaining process variables. When extruding, filaments will be supported by the bottom layer. Increasing the infill percentage, decreases the distance between filament supports therefore reducing filament stretching between supports and increasing the resulting filament width. Increasing printing speed will increase filament stretching, reducing filament width, while increasing layer thickness increases filament rigidity, increasing the resulting filament width [39]. Pore cross-sectional area was also determined in the produced geometries, rendering a comparable trend. In every case attained pore area is higher than the designed value (0.870, 0.160 and 0.029 mm^2, for 30%, 50% and 70% infill respectively). Pore area depends primarily on filament width. For scaffolds printed at 200 °C (Fig. 6c) the lower than expected filament width, due to printing limitations, resulted in higher pore areas when compared with the scaffolds printed at 220 °C (Fig. 6d). The higher geometric compliance on scaffolds printed at 220 °C is expected to result from the decrease of PLA melt viscosity and elasticity [36].

alt-text: Fig. 6

Fig. 6

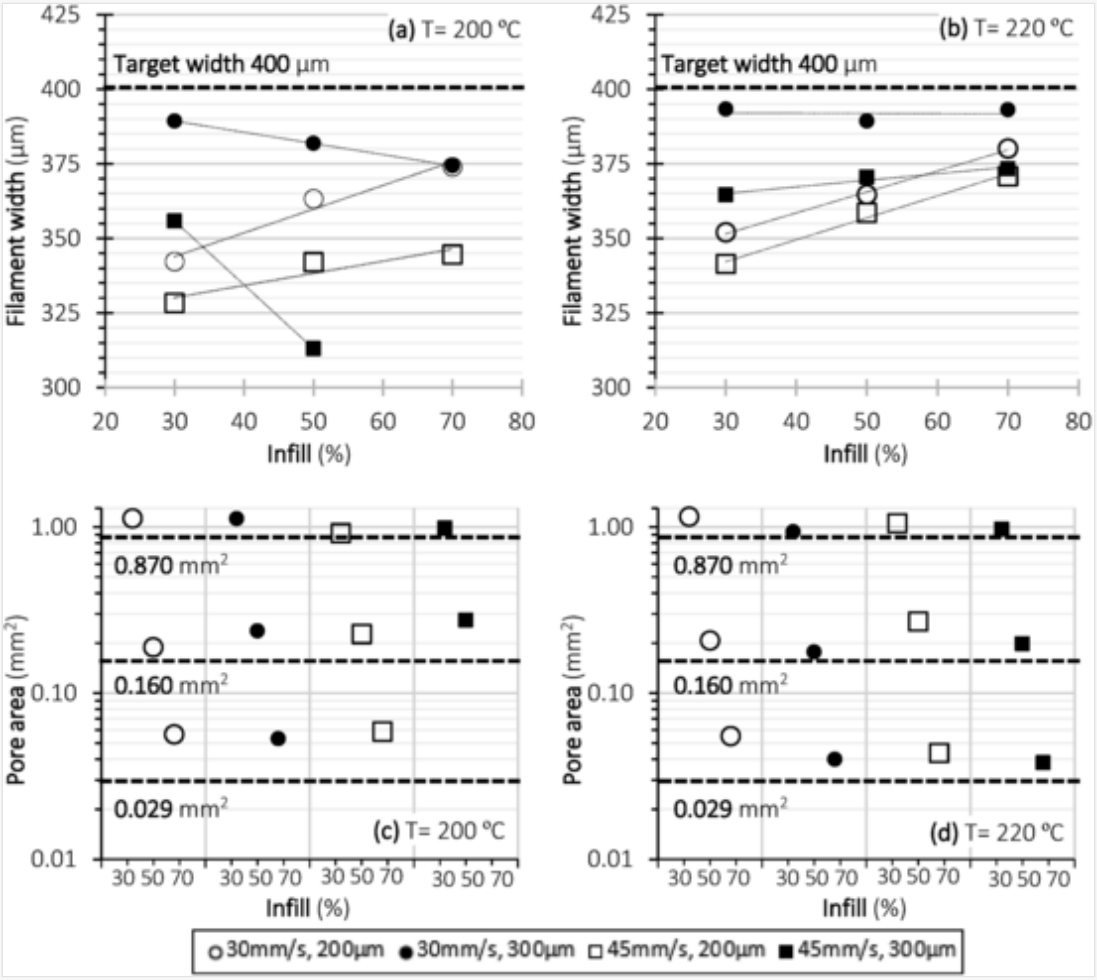

Geometric features of the produced Ortho scaffolds: filament width resulting from FFF at (a) 200 °C and (b) 220 °C; pores cross-sectional area from FFF at (c) 200 °C and (d) 220 °C, produced with different printing speeds (30 mm/s and 45 mm/s) and layer thickness (200 µm and 300 µm).

alt-text: Fig. 7

Fig. 7

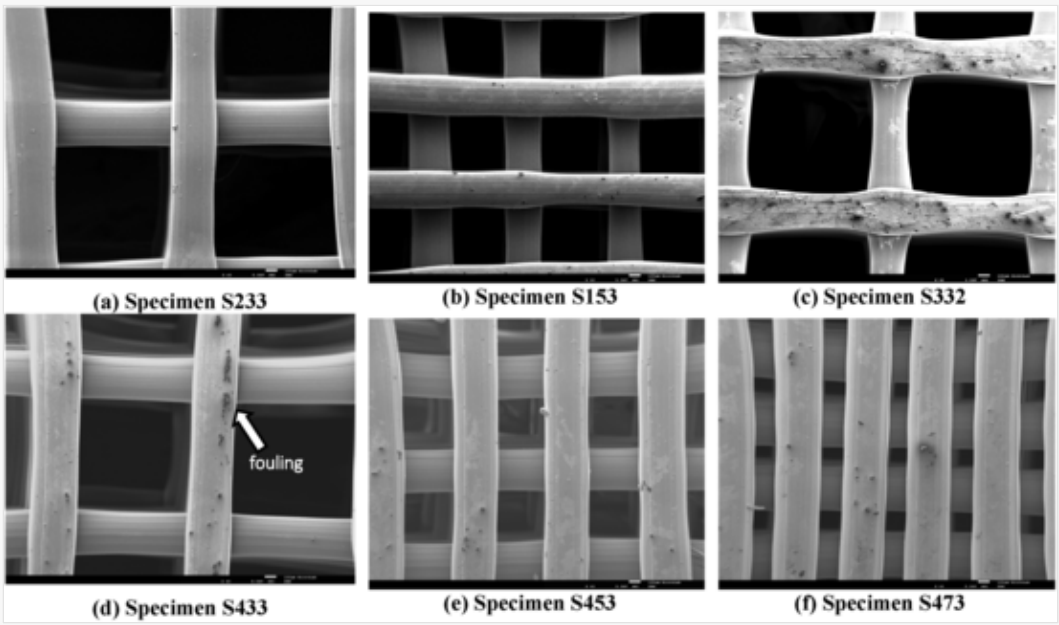

Low magnification images (top view) of produced Ortho scaffolds. FFF at 200 °C: (a) the best geometric compliance was obtained with 30 mm/s, 30%, 300 µm combination; (b) the worse resulted from 45 mm/s, infill 50%, 300 µm. FFF at 220 °C:

(c) the worse geometric compliance was obtained with 45 mm/s, 30%, 200 μm combination; The use of the 30 mm/s, 300 μm combination resulted in the best results, both at (d) 30%; (e) 50%; and (f) 70% tailored infill.

Fig. 7 also draws attention to the effect of thermal degradation of PLA upon FFF processed parts, with extensive fouling visible on the surface of scaffolds printed at 220 °C (Fig. 7c–f). Fouling is directly caused by thermal degradation of PLA above 200 °C [36]: depolymerization results in the formation of monomer and oligomer lactides, that gradually build up on part and equipment surfaces [36].

The produced *Ortho* scaffolds were submitted to monotonic compression tests. Baptista et al. [40] previously reported results on the influence of different manufacturing parameters on mechanical properties for 50% infill scaffolds. The current paper expands that preliminary work for other infill values, illustrating the influence of scaffold porosity on mechanical properties. Fig. 8 shows the three typical compression curves obtained, depending on scaffold infill. The compression curve for porous scaffolds can be divided into four different regions [13]: (1) a region of linear elastic behavior; (2) a region of almost constant stress level, where scaffold deformation increases while stress levels remain constant, due to layer buckling and collapse; (3) a region where the compression slope increases at a higher rate, after the majority of scaffold pores has collapsed [41]; and (4) a final region where stress might decrease as scaffold structure starts to fail and break down. As porosity decreases both the apparent compressive modulus and the yield stress increase. Both compression modulus and yield stress can increase from two-fold, when comparing scaffolds with 30% and 50% infill, up to seven-fold, when comparing an increase from 30% to 70% infill.

alt-text: Fig. 8

Fig. 8

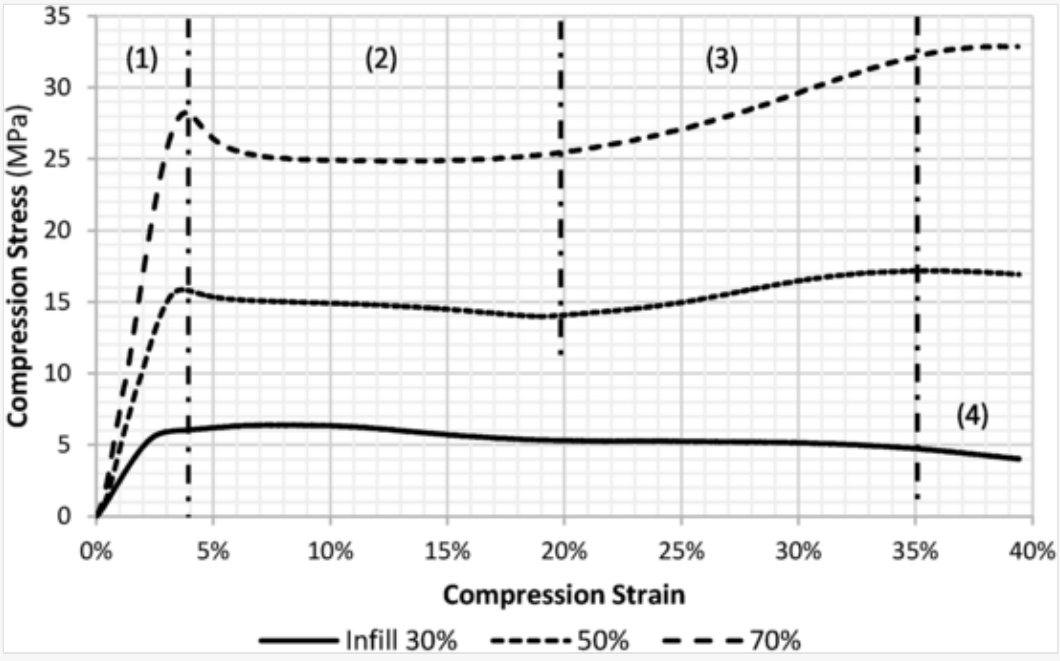

Stress-Strain compression curve for 30%, 50% and 70% infill scaffolds, 3D printed at 220 °C with a 30 mm/s speed and 200 μm layer thickness.

Considering 200 μm layer thickness *Ortho* scaffolds with 30% infill, apparent compressive modulus increased from 212 ± 45 MPa to 257 ± 7 MPa when FFF temperature increased from 200 °C (Fig. 9d) to 220 °C (Fig. 9b) and speed increased from 30 mm/s (Fig. 9d) to 45 mm/s (Fig. 9a). Increasing scaffold infill to 50%, leads to an overall increase in mechanical properties. While printing at 200 °C with a 45 mm/s speed resulted on a

480 ± 5 MPa compressive modulus, increasing the temperature to 220 °C and reducing the printing speed to 30 mm/s, increased the compressive modulus to 555 ± 19 MPa. A similar behavior was obtained for the 70% infill scaffolds, with compressive modulus increasing from 625 ± 68 MPa to 942 ± 22 MPa, in the same conditions.

alt-text: Fig. 9

Fig. 9

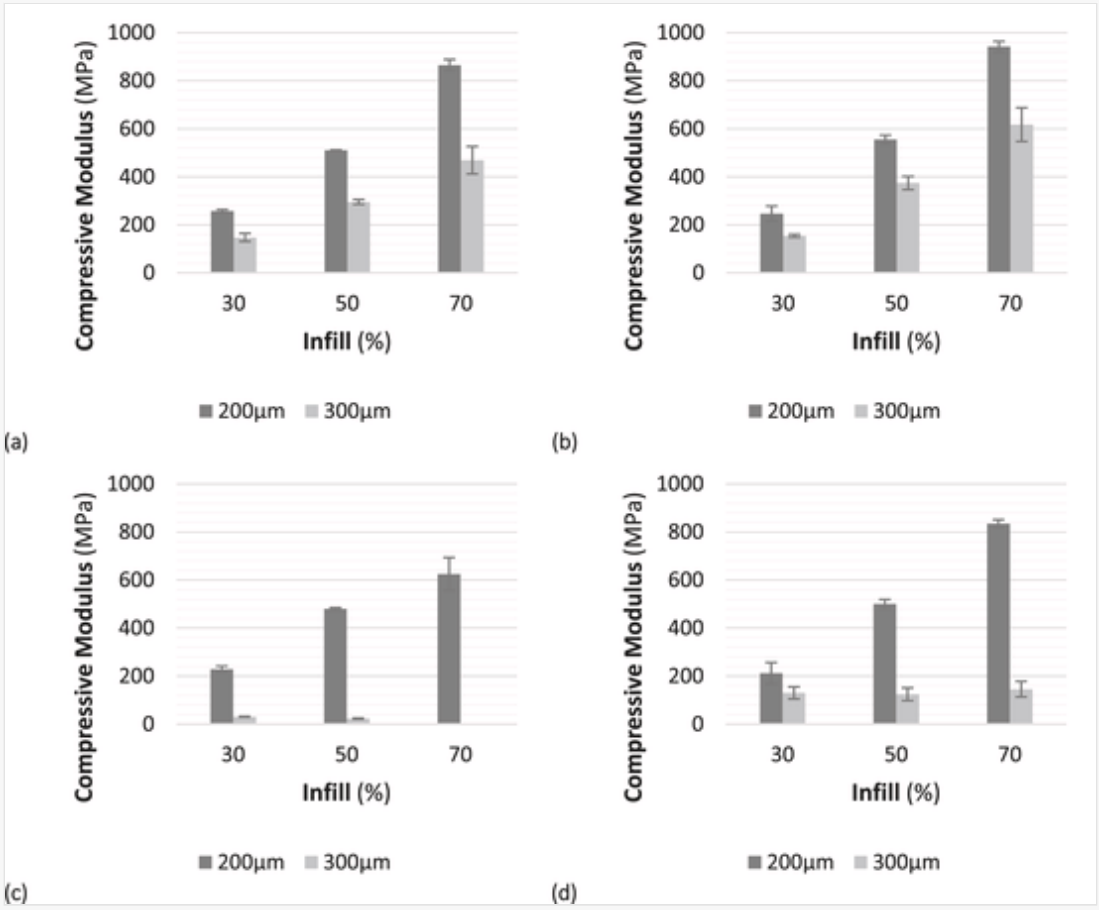

Comparison between different FFF parameters, infill (30%, 50% and 70%) and layer thickness (200 µm and 300 µm) regarding compressive modulus, a) 45 mm/s printing speed and 220 °C printing temperature; b) 30 mm/s and 220 °C; c) 45 mm/s and 200 °C and d) 30 mm/s and 200 °C ortho scaffolds.

Combining 300 µm layer thickness scaffolds with the 200 °C printing temperature, considerably reduces the scaffold's mechanical properties. When printing at the lower temperature and higher speed (45 mm/s), scaffold compressive modulus decreased to a minimum of 23 ± 2 MPa for a 50% infill scaffold, while it was not possible to print the 70% infill scaffold due to lack of material extrusion. Decreasing the printing speed to 30 mm/s, increased the overall mechanical properties, yet compressive modulus showed no statistically significant differences for different infill percentages, reaching a maximum value of 146 ± 22 MPa (Fig. 9d). Mechanical properties for the 300 µm layer thickness scaffolds printed at 220 °C (Fig. 9b), showed similar behavior to the 200 µm layer thickness scaffolds (Fig. 9a), but with inferior values. The minimum value of compressive modulus (148 ± 17 MPa) was obtained for a 45 mm/s speed and 70% porosity, while the maximum value (617 ± 70 MPa) was obtained with 30 mm/s speed and 30% porosity. Rodrigues et al. [13] have obtained similar values for 60% porosity scaffolds, while Germain et al. [12] obtained slightly inferior results when analyzing 70% porosity scaffolds (orthogonal scaffolds design in both reports).

The evolution of scaffold yield stress was very similar. For 200 μm layer scaffolds, yield stress varied from a minimum of 5.5 ± 1.0 MPa (200 °C, 30 mm/s and 70% porosity) to a maximum of 27.8 ± 0.4 MPa (220 °C, 30 mm/s and 30% porosity). For 300 μm layer scaffolds, yield stress values were very modest when printed at 200 °C, reaching a maximum of 19.8 ± 0.3 MPa (200 °C, 30 mm/s and 30% porosity).

It is clear that the preferred manufacturing parameters are obtained when printing at 220 °C (higher temperature) and 30 mm/s (lower printing speed), where the resulting scaffolds showed better mechanical properties. Scaffold layer thickness should be set to 200 μm, in order to achieve improved mechanical properties. Finally, scaffold infill parameter affects both mechanical properties and porosity, therefore it should be tailored according to scaffold specific application.

3.4 Influence of scaffold design

In order to assess scaffold design influence on scaffold morphology and mechanical properties, four different designs (*Ortho*, Fig. 10a, *2xOrtho*, Fig. 10e, *Displ*, Fig. 10b and *2xDispl*, Fig. 10c) were generated and printed using the previously determined preferred manufacturing parameters. Fig. 11 summarizes the geometrical features of produced *Ortho* and *Displ* scaffolds. The measured printed filament width varies considerably depending on scaffold design.

alt-text: Fig. 10

Fig. 10

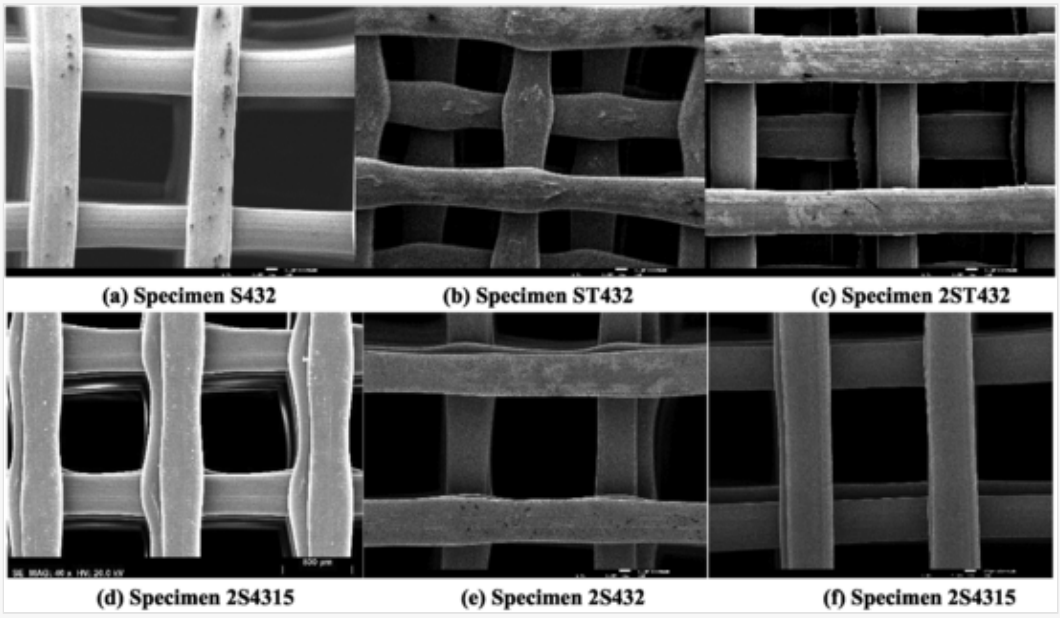

SEM scaffold morphology for different designs; (a) Ortho; (b) Displ and (c) 2xDispl scaffolds, printed with 200 μm layer thickness, and 2xOrtho scaffolds printed with (d) 150 μm, (e) 200 μm and (f) 300 μm, 30 mm/s speed and 220 °C printing temperature.

alt-text: Fig. 11

Fig. 11

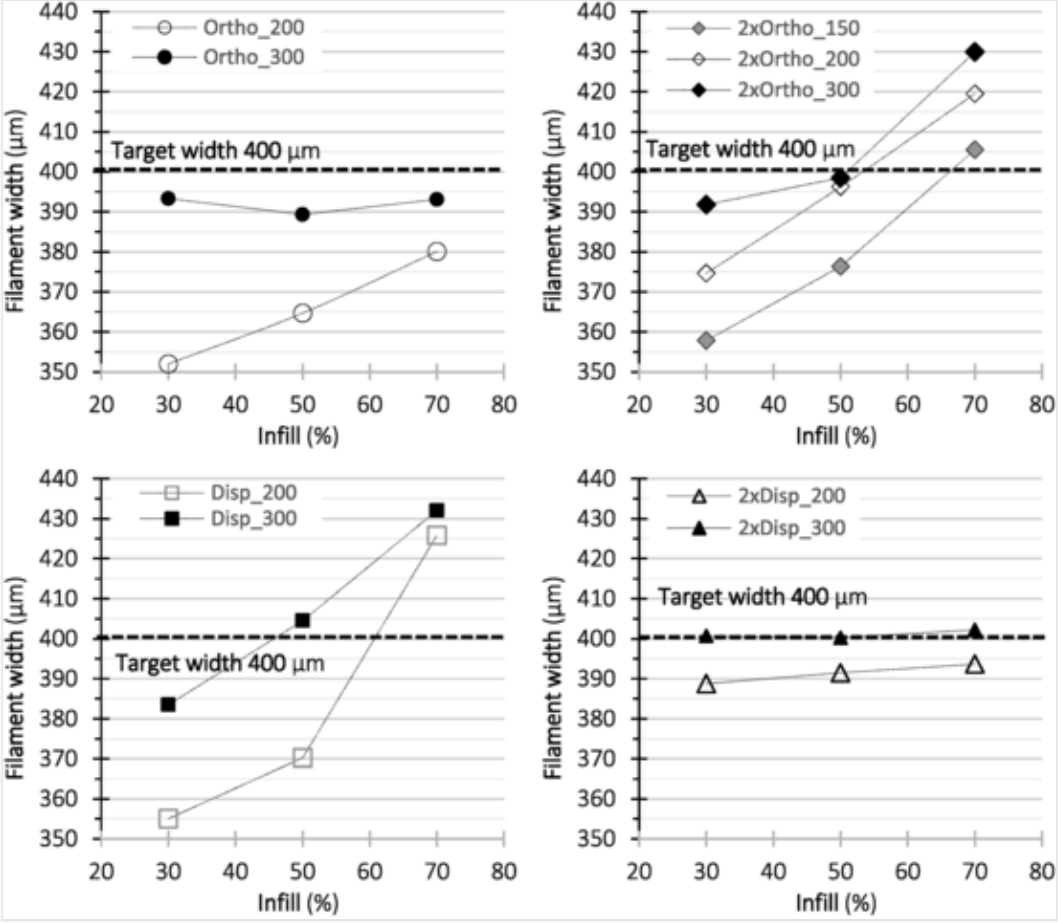

Comparison of geometric features of scaffolds printed at 220 °C at 30 mm/s with (a) Ortho; (b) 2xOrtho; (c) Disp; and (d) 2xDisp geometry, with different layer thickness (200 µm and 300 µm).

Overall, *Ortho* (Fig. 11a) and *Disp* (Fig. 11c) designs appear to result in higher scattering of filament width values, respectively ranging from to 352 ± 38 µm (30% infill, 200 µm tailored thickness) to 393 ± 16 µm (70%, 300 µm), and from 355 ± 53 µm (30%, 200 µm) to 432 ± 17 µm (70%, 300 µm). Regardless of designed pattern and of tailored thickness, filament width appears to increase with infill percentage. At 70% infill, except for *Ortho* samples, all geometries display filament width higher than the used nozzle diameter (400 µm). The deviation is of 4.6% and 7.0% for *2xOrtho* samples respectively aimed at 200 µm and 300 µm filament thickness, and of 6.1% and 7.4% for *Disp s*amples aimed at 200 µm and 300 µm filament thickness. In these cases, geometric compliance with nozzle dimensions is higher at 50% infill. The 2x*Disp s*amples show the higher compliance with nozzle diameter, with a variation of −1.6% at 200 µm and of 0.6% at 300 µm. 3D printing scaffolds with a lower layer thickness (150 µm, Fig. 10d) showed that filament width is proportional this parameter (Fig. 10d–f and Fig. 11b). When compared against scaffolds with similar lateral pore dimension (300 µm *Ortho*), filament width may decrease up to 10%. No significant statistical variance was found between scaffold designs. Therefore, filament width is only a function of process parameters, as shown in the previous section. Scaffolds pore cross-sectional area was also evaluated. Fig. 12 show the resulting pore area reduction when using the staggered (*Displ*) configuration.

alt-text: Fig. 12

Fig. 12

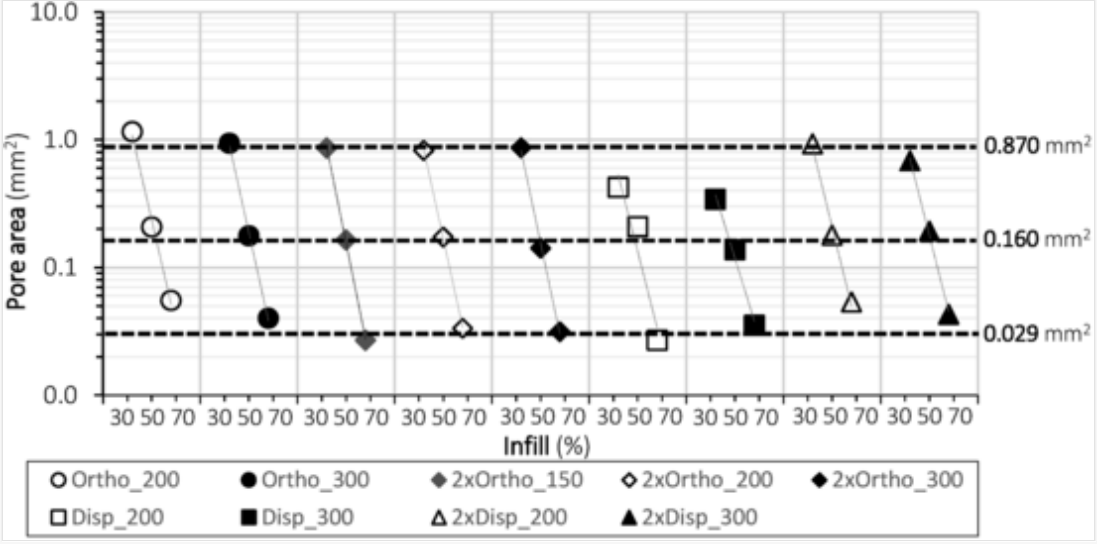

Pores cross-sectional area (FFF at 220 °C and 30 mm/s) for scaffolds with different layer thickness (150 μm, 200 μm and 300 μm).

Regarding scaffold mechanical properties, Fig. 13 shows the influence of scaffold design on apparent compressive modulus and yield stress. Staggered configurations show decreased mechanical properties, when compared with aligned scaffolds. Using a double layer configuration, increased both scaffold compressive modulus and yield stress.

alt-text: Fig. 13

Fig. 13

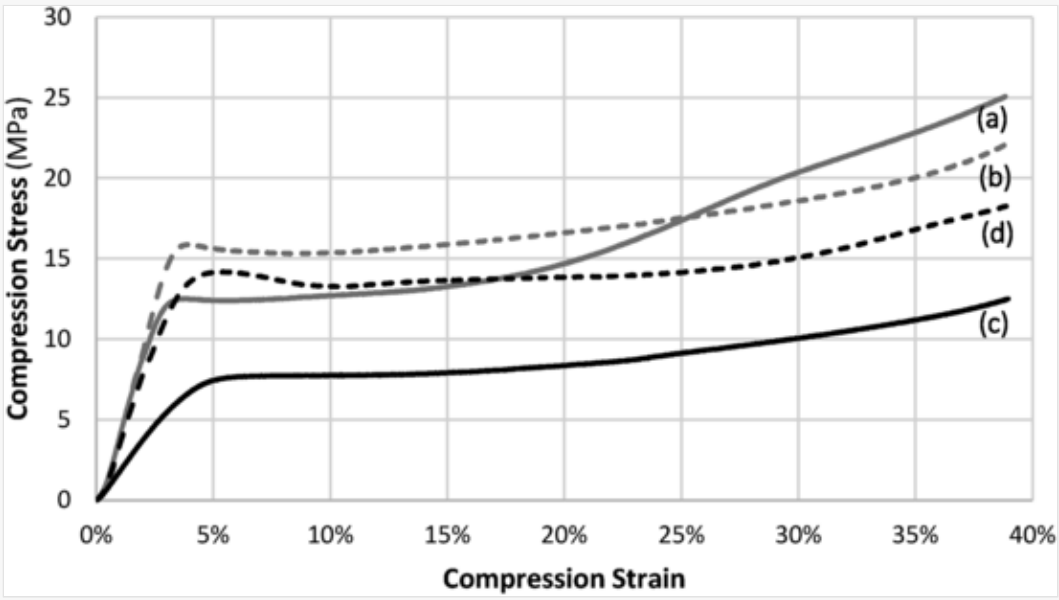

Stress-Strain compression curves for different scaffold designs (a) Ortho, (b) 2xOrtho, (c) Displ and (d) 2xDispl, 3D printed at 220 °C, with 30 mm/s speed and 200 μm layer thickness.

Fig. 13 shows the obtained differences between *Ortho* a), *2xOrtho* b), *Displ* c) and *2xDispl* d) scaffolds. 3D printing speed and temperature were constant (220 °C and 30 mm/s), while layer thickness also varied from 200 to 300 μm. As expected, decreasing scaffold porosity, increased mechanical properties, on all four different

scaffolds' designs. The layer design, single or double layer, also showed major influence on scaffold behavior. While single layer *Ortho* scaffold compressive modulus varied from 133 ± 1 MPa (70% porosity, 300 μm) to 918 ± 31 MPa (30% porosity, 200 μm), double layer *2xOrtho* scaffold compressive modulus increased to a minimum of 211 ± 5 MPa and a maximum of 1018 ± 13 MPa. A similar behavior was found for staggered configurations, *Displ* and *2xDispl* scaffolds. Compressive modulus minimum values were obtained for 30% infill scaffolds, with 200 μm layer, increasing from 31 ± 1 MPa to 90 ± 2 MPa. While maximum values were obtained for 70% infill scaffolds, also with 200 μm layers, increasing from 653 ± 7 MPa to 919 ± 5 MPa. Finally, layer thickness was also assessed. Fig. 14 shows that increasing layer thickness decreased the *Ortho* and *2xOrtho* scaffold mechanical properties, while not affecting the mechanical properties on the majority of the *Displ* and *2xDispl* scaffolds configurations. Fig. 14 d) shows the configurations where significant statistical differences were found (*2xDispl* scaffold with 70% infill). For these configurations, increasing layer thickness also leads to a decrease in mechanical properties.

alt-text: Fig. 14

Fig. 14

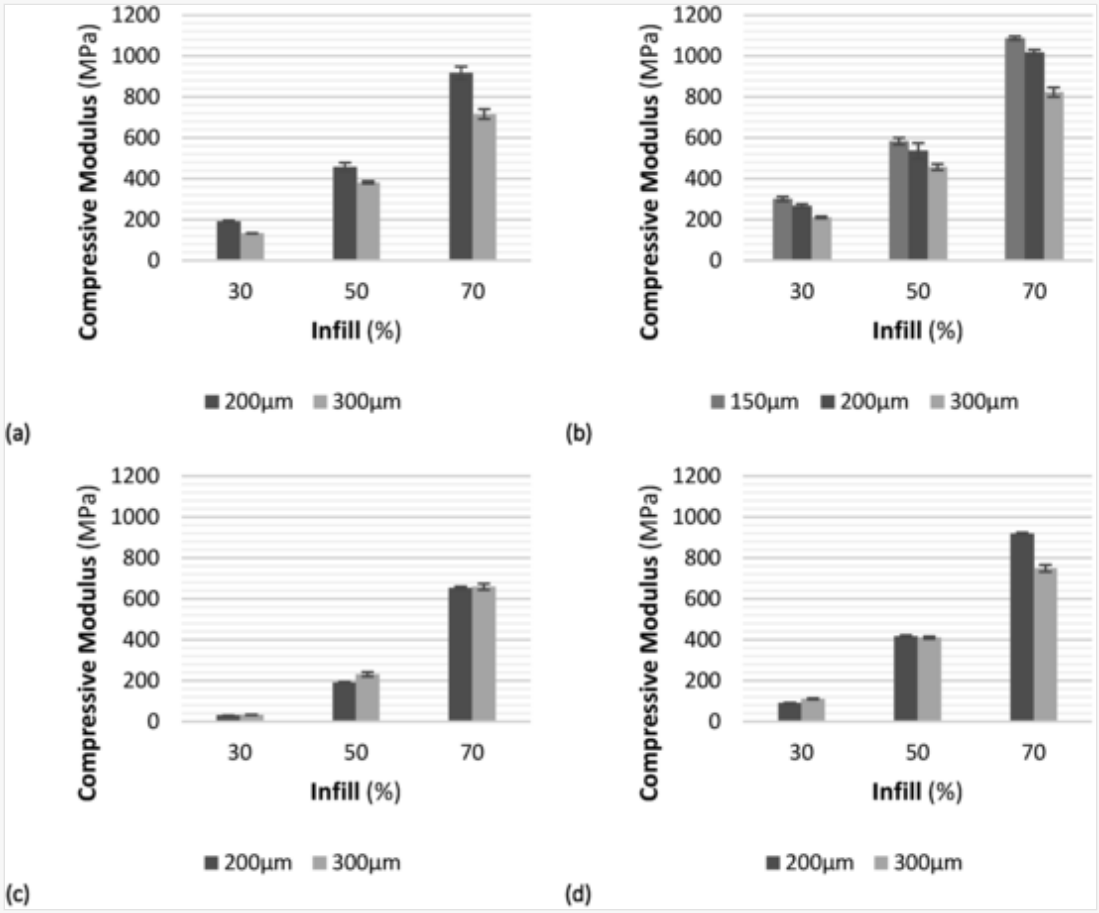

Comparison between different scaffolds geometries, layer thickness and porosities regarding compressive modulus, a) Ortho; b) 2xOrtho; c) Displ and d) 2xDispl scaffolds.

Overall staggered configurations shown reduced mechanical properties. Both Gregor et al. [3] and Navarro et al. [42] reported compressive modulus reduction from 50% to 70%, when using staggered scaffolds designs. Fig. 14 shows an average 49% decrease on the compressive modulus of *Displ* vs *Ortho* scaffolds, with a major difference between 192 ± 4 MPa and 31 ± 1 MPa (−84%) for 30% infill, 200 μm scaffolds and a minor difference between 749 ± 16 MPa and 659 ± 16 MPa (−8%) for 70% infill, 300 μm scaffolds.

A special *2xOrtho* scaffold configuration was also printed with a 150 μm layer thickness. Therefore, these scaffolds lateral pore dimension (300 μm) is equal to the 300 μm *Ortho* scaffold. Fig. 14b shows an increased mechanical performance when scaffold's layer thickness is reduced (301 ± 11 MPa to 1088 ± 9 MPa, as scaffold infill increases from 30 to 70%). When compared to the corresponding properties of the 300 μm single layer scaffold, apparent compressive modulus increases up to 2.3-fold, for the same lateral pore dimension.

Scaffold yield stress followed the same behavior as compressive modulus. Orthogonal scaffolds minimum yield stress was 3.5 ± 0.1 MPa, for the *Ortho*, 30% infill, 300 μm scaffold, while the maximum yield stress was 30.3 ± 0.3 MPa, for the *2xOrtho*, 70% infill, 150 μm scaffold. Staggered configuration showed inferior yield stress levels, with the minimum value of 1.1 ± 0 0.1 MPa, for the *Displ*, 30% infill, 200 μm scaffold, and the maximum value reaching 27.6 ± 0.1 MPa, for the *2xDispl*, 70% infill, 200 μm scaffold.

3.5 Micro-CT porosity analysis

In order to assess scaffold porosity and pore interconnectivity, *Ortho* scaffolds printed with the preferred manufacturing parameters were analyzed by μ-CT [43]. Table 5 shows obtained values before mechanical compression and after 40% strain compression test. Differences between theoretical values and experimentally determined values are within the same range as obtained by Germain et al. [12]. Open porosity is very close to 100%, suggesting that all pores are interconnected, which is mandatory for bone replacement scaffolds. After 40% compression and load removal, there is an 8–24% decrease in porosity. This decrease is a consequence of pore collapse and increases as filament offset distance decreases. Nevertheless, the remaining pores are still fully interconnected. Fig. 15 shows scaffold morphology and pores distribution for the three different *Ortho* scaffold porosities. As mentioned, decreasing the pore size (by increasing scaffold infill percentage) will increase the scaffold's surface area. Measured using surface density parameter (scaffold surface divide by total analyzed volume), Table 5 shows an increase from 3.03 mm^2/mm^3 to 5.03 mm^2/mm^3, as scaffold infill increases. Once deformed, pore collapse will lead to a surface density decrease.

alt-text: Table 5

Table 5

The table layout displayed in this section is not how it will appear in the final version. The representation below is solely purposed for providing corrections to the table. To preview the actual presentation of the table, please view the Proof.

Micro-CT measured scaffolds porosities, percentage of interconnected (open) pores and surface density on ortho scaffolds with different theoretical porosities.

	Scaffold Infill	30%	50%	70%
Untested	Porosity (%)	67.7	49.2	32.7
	Open porosity (%)	100.0	99.9	99.7
	Surface density (mm^2/mm^3)	3.03	4.28	5.03
Tested	Porosity (%)	62.2	43.5	24.9
	Open porosity (%)	100.0	100.0	99.8
	Surface density (mm^2/mm^3)	2.96	3.53	3.42

alt-text: Fig. 15

Fig. 15

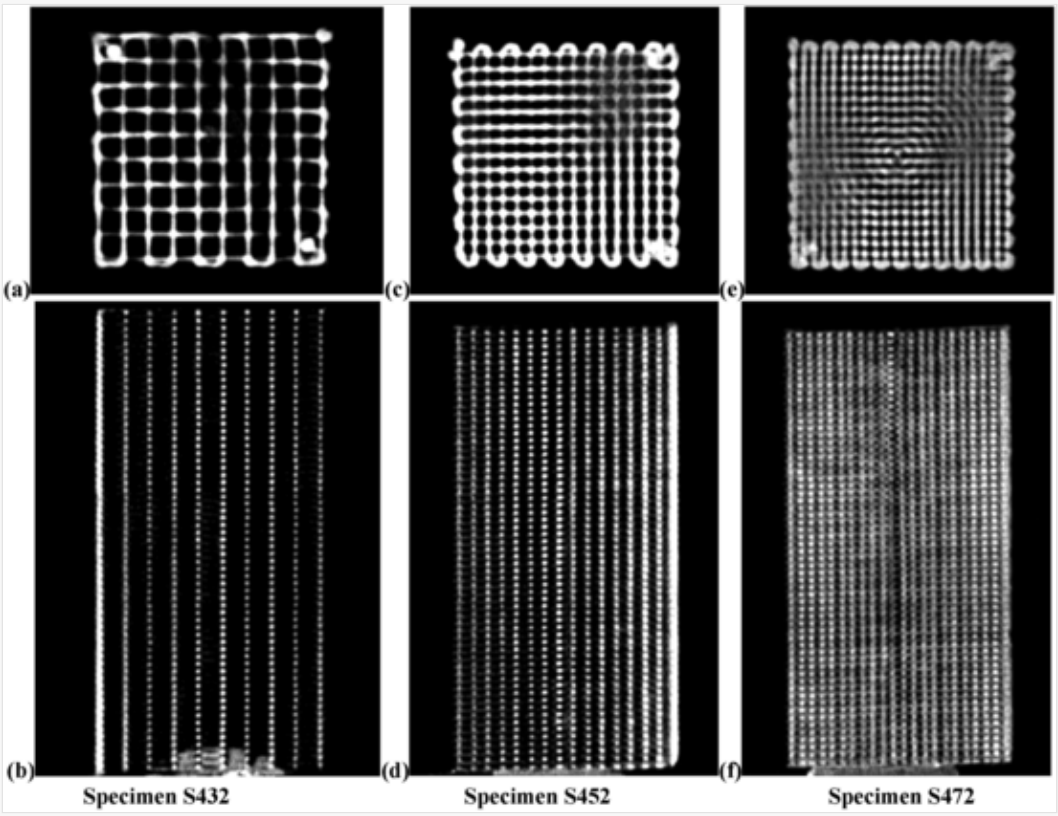

a) axial view and b) coronal view of an Ortho scaffold with 30% infill; c) axial view and d) coronal view of an Ortho scaffold with 50% infill; and e) axial view and f) coronal view of an Ortho scaffold with a 70% infill.

4 Discussion and conclusions

Porous thermoplastic scaffolds can be used to replace bone tissue, after trauma, disease or damage, as long as several characteristics are ensured while bone tissue regenerates, mainly biocompatibility, fully interconnected porous structure and ability to withstand mechanical loads [4]. In this context PLA scaffolds were 3D printed using FFF manufacturing technique, with the goal of determining the manufacturing parameters and scaffold design influence upon specimen morphology and final mechanical performance. Scaffold designs were customized, including variable layer thickness, printing speed, printing temperature and filament offset distance.

Scaffold porous structure was analyzed by Micro-CT scanning. Three scaffolds with different infill parameters were selected, after determining the preferred manufacturing parameters. When analyzing an *Ortho* scaffold with 30% infill, Micro-CT determined scaffold porosity (67.7%) was very close to the theoretical value (70%). All the pores were open, which means that a fully interconnected pore structure was achieved with our manufacturing methodology. After 40% strain compression and stress removal, the porosity of this scaffold was 62.2%, as measured by Micro-CT, and all pores remained open. This suggests that although some pores have collapsed by the applied deformation, all the remaining pores are still fully interconnected. Table 5 shows similar behaviors for the 50% infill and 70% infill scaffolds. After compression, lower porosity scaffolds show a higher number of closed pores. Lower porosity scaffolds were achieved by reducing the pore size, therefore by applying the same deformation, more pores will be closed, due the filament transverse deformation. Still, even after compression testing, Micro-CT shows that different porosity scaffolds pores will be fully interconnected.

Therefore, using FFF to manufacture PLA scaffolds is a viable strategy. Porosity influences both cell attachment and growth, and scaffold mechanical properties [1,2,6,7], and can be fine-tune by using different manufacturing parameters [39]. Micro-CT analysis showed that surface density is influenced by porosity. Increasing porosity, reduces scaffold pore size and increases surface density, allowing for more interaction sites between scaffold and cells, improving cell attachment and growth.

Current work shows that selecting the ideal manufacturing parameters is essential to obtain higher mechanical properties and provides a guide for tailoring these properties according to different applications. Manufacturing parameters' influence on scaffold morphology and mechanical properties can be analyzed from a printability model perspective, which depends on rheological and thermo-physical material properties [31]. Thus, printability depends on the FFF printer ability to develop the necessary pressure to extrude the designed amount of material and also on the material ability to form strong connections between printed layers. Fig. 3 shows that material viscosity is highly dependent on FFF temperature. As temperature increases, PLA viscosity decreases, lowering the necessary pressure to extrude and print scaffolds. At 220 °C PLA viscosity and shear rate show typical power-law fit, while at 200 °C there is clear transition between Newtonian and power-law behaviors (Fig. 3). In order to calculate the total amount of pressure need to extrude PLA through the nozzle the Rabinowitsch model was used in conjunction with the power-law model. The resulting pressure depends on the printing temperature, speed and chosen layer thickness. When trying to print with demanding conditions (low temperature, high speed and layer thickness) pressure rises to 23′945 Pa, leading to nozzle clogging due to the 3D printer inability to extrude the filament or due to filament buckling [31]. Temperature plays a major role, and by increasing temperature to 220 °C, the resulting pressure decreases to 14′645 Pa. By reducing printing speed to 30 mm/s and layer thickness to 200 μm, pressure reduces to 7′420 Pa, resulting in high quality scaffolds. This analysis also showed that the necessary pressure to extrude the filament comes from the final part of the nozzle, where the filament diameter reaches the minimum value (400 μm), while the nozzle entrance only contributed with around 5–10% of the total pressure, reaching 20% when the printing parameter become more demanding (Table 4). Therefore, selecting the correct nozzle exit diameter can also be an important manufacturing parameter, and it might be possible to print at lower temperatures, while using a higher nozzle exit diameter to lower the total amount of pressure necessary to extrude the filament. PLA high printing temperatures are then a material disadvantage, when compared with other biocompatible polymers like PCL. Szojka et al. [44] and Domingos et al. [39] have successfully 3D printed PCL scaffolds using similar designs and porosities, while Serra et al. [42] have combine PEG and PLA polymers, reducing the printing temperature, to obtain high resolution scaffolds with fully fused support points.

The length of the chain is the main factor determining the rheology, although many others are also influential [34]. A long chain will occupy a great deal of space compared to its atomic dimensions. The possibility of polymer molecules linking together temporarily by intermolecular forces increases still further the space over which the influence of an individual molecule is felt. If the polymer chain is long enough, the intermolecular association known as entanglement occurs. The entangled polymer, gives rise to the effects of high elasticity, such as normal stresses and high extensional viscosity [34].

Figs. 6 and 11 show that filament width also depends on FFF processing parameters. When printing with demanding parameters (200 °C, 45 mm/s and 300 μm) filament width was inversely proportional to the infill parameter, and it was not possible to print the scaffold configuration with 70% infill. This is justified by the high values of necessary pressure to extrude the filament, leading to nozzle clogging. Fig. 9c and d also show that printing *BQ* PLA filament at 200 °C with a layer thickness of 300 μm lead to very poor mechanical properties. This is attributed to low adhesion between scaffold layers. In this case the printer must extrude a high amount of

material, at low temperature. When depositing the top layer, support points are fused with the bottom layer, but at low temperature and while extruding high material quantities, the energy density is not enough for the complete fusion between layers, reducing the mechanical properties. For the remaining configurations Fig. 6 shows that filament width is proportional to scaffold infill and layer thickness, but inversely proportional to printing speed. Domingos et al. [39] have also analyzed this problem, on bioprinted PCL scaffolds. While printing, the filament is suspended between a fixed point and the moving nozzle. Increasing printing speed will lead to filament stretching and reduced filament width. Increasing scaffold infill, reduces the filament offset distance and the support points will be closer, filament stretching is reduced and therefore, filament width will increase. Finally, layer thickness increase will increase filament rigidity and reduce filament stretching. Analyzing Fig. 6c and d one can verify that pore area is a function of the resulting filament width. As the final filament width was inferior to the theoretical value, pore areas were higher than expected. The final mechanical properties, apparent compressive modulus (Fig. 9) and yield stress, were well correlated with the filament width. Increasing temperature and scaffold infill and reducing printing speed will lead to higher mechanical properties, with scaffold apparent compressive modulus reaching 942 MPa and yield stress 27.8 MPa for the preferred manufacturing parameters (220 °C, 30 mm/s, 200 μm and 70% infill). Although higher filament width will lead to higher mechanical properties, due to higher contact areas between layers, layer thickness is also important. Our work shows that increasing layer thickness will result in lower mechanical properties. This might be connected to poorer adhesion between layers (as previously explained) or due to structural buckling, resulting from higher columns length [41].

Finally, in this paper, scaffold design influence on mechanical properties was also explored. Four different configurations were developed, by using a double layer configuration and by staggering filaments between layers. Fig. 14 show that staggered configurations (*Displ*) have lower mechanical properties, but lower pore areas which will provide better cell support by limiting cell vertical movement. Poorer mechanical properties are justified by the introduction of bending between support points. Loads are now transferred between layer on an offset position, increasing scaffold overall deformation and reducing apparent compressive modulus and yield stress [42]. This problem might be solved by increasing layer thickness, increasing filament bending rigidity, or by printing scaffolds on a double layer configuration. In this case one will also get an improved adhesion between layers, increasing the overall scaffold mechanical properties. By 3D printing with the preferred parameters a *2xOrtho* scaffold with 70% infill and 150 μm layer thickness it was possible to obtain the maximum value of 1′088 MPa for the scaffold apparent compressive modulus and yield stress of 30.3 MPa. A special 150 μm layer thickness *2xOrtho* scaffold configuration was printed in order to isolate scaffold's lateral pore dimension influence on mechanical properties. These scaffolds lateral pore (300 μm), is equal to the single layer 300 μm layer thickness *Ortho* scaffolds. Our results showed that while increasing layer thickness, decreases both scaffold yield stress and apparent compressive modulus, using a double layer configuration, increases scaffold's mechanical properties. Therefore, when comparing a single layer scaffold with a higher layer thickness, with a double layer scaffold with a lower layer thickness, but with the same lateral pore dimension, one should expect the second configuration to display a higher yield stress and apparent compressive modulus. This behavior was verified when comparing 300 μm *Ortho* with 150 μm *2xOrtho* scaffold's apparent compressive modulus, where a maximum 2.3-fold gain was obtained for lower infill percentage scaffolds. This direct comparison of scaffolds with the same lateral pore dimension, allowed for a clear understanding of the layer thickness and layup design influence on scaffold's mechanical behavior.

Our results show that PLA outperforms both acrylic-based polymers and PCL. When compared with resin-based cured lattice scaffolds, our results show a significantly higher performance. Scaffolds printed with 400 μm beam

diameter, using resin-based cured lattices, and 50 or 30% infill, showed 60.6 and 27.8 MPa apparent compressive modulus respectively [8]. While our results show that when 3D printing equivalent PLA scaffolds, with 400 μm filament diameter and scaffold infill percentages, apparent compressive modulus increases to 458 (specimens S432) and 192 MPa (specimens S452) respectively. While our work shows that increasing layer thickness decreases mechanical performance, Egan et al. showed that acrylic-based polymers scaffold's performance can be improved, increasing beam diameter [8]. When compared with PCL printed scaffolds, our results show that PLA can be used as a higher performance material. Schipani et al. experimental tests on similar *Ortho* aligned PCL scaffolds, with infill percentages between 20 and 40%, resulted on an average 25 MPa apparent compressive modulus [45]. Similar modulus reduction behavior was also found when using displaced scaffolds designs. While Domingos et al. [39] achieved apparent compressive modulus up to 80 MPa for 50% infill PCL scaffolds, our results shows that PLA outperforms PCL with an equivalent value of 458 MPa. Increasing bioprinting temperature, reducing printing speed and layer thickness, allows for higher mechanical properties, in the same fashion as FFF printing.

Overall this paper shows that FFF 3D printing of PLA scaffolds is a viable manufacturing process. Different designs of porous structures with full interconnectivity were achieved. Even after 40% compressive deformations the pores remains fully interconnected, allowing for cell oxygenation and nutrient diffusion. Compressive deformation reduces scaffold porosity, due to pore collapse, but scaffold infill parameter allows to tailor scaffold porosity to specific applications. 3D printing parameters are very important for scaffold final morphology and mechanical properties. Reducing printing temperature and increasing printing speed and layer thickness, increases the necessary pressure to extrude the filament, leading to nozzle clogging and reduced filament width. This affects the scaffold mechanical properties. Therefore, ideal 3D printing conditions include high printing temperatures and low printing speeds, in order to increase filament width, and to reduce layer thickness to increase scaffold mechanical properties. Scaffold infill also affects mechanical performance, controlling porosity and filament width. This parameter should be used to tailor scaffolds for the required application.

CRediT authorship contribution statement

R. Baptista: Conceptualization, Methodology, Formal analysis, Investigation, Resources, Writing - original draft, Visualization, Supervision. **M. Guedes:** Methodology, Validation, Formal analysis, Investigation, Resources, Writing - original draft, Writing - review & editing. **M.F.C. Pereira:** Methodology, Investigation, Resources, Writing - review & editing. **A. Maurício:** Investigation, Resources, Data curation, Visualization. **H. Carrelo:** Investigation, Resources, Data curation, Visualization. **T. Cidade:** Methodology, Validation, Investigation, Resources, Writing - review & editing.

Declaration of competing interest

The authors declare that they have no known competing financial interests or personal relationships that could have appeared to influence the work reported in this paper.

Acknowledgments

This work was supported by FCT, through IDMEC under LAETA, project UIDB/50022/2020, CeFEMA contract UID/CTM/04540/2019, Strategic Project Pest-C/CTM/LA0025/2011 and CERENA Strategic Project UIDB/04028/2020.

Appendix A Supplementary data

Supplementary data to this article can be found online at https://doi.org/10.1016/j.bprint.2020.e00096.

References

The corrections made in this section will be reviewed and approved by a journal production editor. The newly added/removed references and its citations will be reordered and rearranged by the production team.

[1] Turnbull G., Clarke J., Picard F., Riches P., Jia L., Han F., Li B., Shu W., 3D bioactive composite scaffolds for bone tissue engineering, Bioact. Mater. 3 (2018) 278–314, doi:10.1016/j.bioactmat.2017.10.001.

[2] Yang S., Leong K.-F., Du Z., Chua C.-K., The design of scaffolds for use in tissue engineering. Part I. Traditional factors, Tissue Eng. 7 (2001) 679–689, doi:10.1089/107632701753337645.

[3] Gregor A., Filová E., Novák M., Kronek J., Chlup H., Blahnová V., Barto M., Ne A., Ho J., Buzgo M., Blahnová V., Lukášová V., Bartoš M., Nečas A., Hošek J., Designing of PLA scaffolds for bone tissue replacement fabricated by ordinary commercial 3D printer, J. Biol. Eng. 11 (2017) 1–21, doi:10.1186/s13036-017-0074-3.

[4] Roseti L., Parisi V., Petretta M., Cavallo C., Desando G., Bartolotti I., Grigolo B., Scaffolds for bone tissue engineering: state of the art and new perspectives, Mater. Sci. Eng. C 78 (2017) 1246–1262, doi:10.1016/j.msec.2017.05.017.

[5] Chia H.N., Wu B.M., Recent advances in 3D printing of biomaterials, J. Biol. Eng. 9 (2015) 4, doi:10.1186/s13036-015-0001-4.

[6] Li X., Wang L., Fan Y., Feng Q., Cui F.-Z., Watari F., Nanostructured scaffolds for bone tissue engineering, J. Biomed. Mater. Res. 101A (2013) 2424–2435, doi:10.1002/jbm.a.34539.

[7] Lu J.X., Flautre B., Anselme K., HAardouin P., Gallur A., Descamps M., Thierry B., Role of interconnections in porous bioceramics on bone recolonization in vitro and in vivo, J. Mater. Sci. Mater. Med. 10 (1999) 111–120.

[8] Egan P.F., Bauer I., Shea K., Ferguson S.J., Mechanics of three-dimensional printed lattices for biomedical devices, J. Mech. Des. Trans. ASME. 141 (2019) 1–12, doi:10.1115/1.4042213.

[9] Tappa K., Jammalamadaka U., Novel biomaterials used in medical 3D printing techniques, J. Funct. Biomater. 7 (2018).

[10] Gibson I., Rosen D., Stucker B., Additive Manufacturing Technologies, second ed., Springer Science & Business Media, New York, 2015.

[11] Grémare A., Guduric V., Bareille R., Heroguez V., Latour S., L'heureux N., Fricain J.C., Catros S., Le Nihouannen D., Characterization of printed PLA scaffolds for bone tissue engineering, J. Biomed. Mater. Res. 106 (2018) 887–894, doi:10.1002/jbm.a.36289.

[12] Germain L., Fuentes C.A., van Vuure A.W., des Rieux A., Dupont-Gillain C., 3D-printed biodegradable gyroid scaffolds for tissue engineering applications, Mater. Des. 151 (2018) 113–122, doi:10.1016/j.matdes.2018.04.037.

[13] Rodrigues N., Benning M., Ferreira A.M., Dixon L., Dalgarno K., Manufacture and characterisation of porous PLA scaffolds, Procedia CIRP, 2016, pp. 33–38, doi:10.1016/j.procir.2015.07.025.

[14] Gleadall A., Visscher D., Yang J., Thomas D., Segal J., Review of additive manufactured tissue engineering scaffolds: relationship between geometry and performance, Burn, Trauma 6 (2018) 19, doi:10.1186/s41038-018-0121-4.

[15] Yang T., Hu Y., Wang C., Binks B.P., Fabrication of hierarchical macroporous biocompatible scaffolds by combining pickering high internal phase emulsion templates with three-dimensional printing, ACS Appl. Mater. Interfaces 9 (2017) 22950–22958, doi:10.1021/acsami.7b05012.

[16] Perego G., Cella G.D., Mechanical Properties, Poly(Lactic Acid), 2010, pp. 141–153, doi:10.1002/9780470649848.ch11.

[17] Burg K., Poly(α-ester)s, Nat. Synth. Biomed. Polym. (2014) 115–121, doi:10.1016/B978-0-12-396983-5.00006-5.

[18] Kister G., Cassanas G., Vert M., Pauvert B., Térol A., Vibrational analysis of poly(L-lactic acid), J. Raman Spectrosc. 26 (1995) 307–311, doi:10.1002/jrs.1250260409.

[19] Kister G., Cassanas G., Vert M., Effects of morphology, conformation and configuration on the IR and Raman spectra of various poly(lactic acid)s, Polymer 39 (1998) 267–273, doi:10.1016/S0032-3861(97)00229-2.

[20] Ross G., Ross S., Tighe B.J., Bioplastics: new routes, new products, Brydson's Plast. Mater., Butterworth-Heinemann, 2017, pp. 631–652, doi:10.1016/B978-0-323-35824-8.00023-2.

[21] Müller A.J., Ávila M., Saenz G., Salazar J., Crystallization of PLA-based materials, in: Jiménez A., Peltzer M., Ruseckaite R. (Eds.), Poly(Lactic Acid) Sci. Technol. Process. Prop. Addit. Appl., The Royal Society of Chemistry, 2015, pp. 66–98.

[22] Suzuki S., Ikada Y., Medical applications, in: Grossman R.F., Nwabunma D., Auras R., Lim L., Selke S.E., Tsuji H. (Eds.), Poly(Lactic Acid), 2010, pp. 445–456.

[23] Jia W., Luo Y., Yu J., Liu B., Hu M., Chai L., Wang C., Effects of high-repetition-rate femtosecond laser micromachining on the physical and chemical properties of polylactide (PLA), Optic Express 23 (2015) 26932–26939, doi:10.1364/OE.23.026932.

[24] Cassanas G., Kister G., Fabrègue E., Morssli M., Bardet L., Raman spectra of glycolic acid, l-lactic acid and d,l-lactic acid oligomers, Spectrochim. Acta Part A Mol. Spectrosc. 49 (1993) 271–279, doi:10.1016/0584-8539(93)80181-9.

[25] Gregorova A., Application of differential scanning Calorimetry to the characterization of biopolymers, in: Elkordy A.A. (Ed.), Appl. Calorim. A Wide Context –Differential Scanning Calorimetry, Isothermal Titration Calorim. Microcalorim., InTech, 2013, pp. 1–20.

[26] Jia S., Yu D., Zhu Y., Wang Z., Chen L., Fu L., Morphology, crystallization and thermal behaviors of PLA-based composites: wonderful effects of hybrid GO/PEG via dynamic impregnating, Polymers 9 (2017) 528–547.

[27] Fischer E.W., Sterzel H.J., Wegner G., Investigation of the structure of solution grown crystals of lactide copolymers by means of chemical reactions, Kolloid-Z. Z. Polym. 251 (1973) 980–990, doi:10.1007/BF01498927.

[28] Wojdyr M., Fityk: a general-purpose peak fitting program, J. Appl. Crystallogr. 43 (2010) 1126–1128.

[29] Saito T., Structure-dependent performances in the electronic applications of single-wall carbon nanotubes, Proc. C. Emerg. Technol. Res. Conf., Canada, Vancouver, 2015, pp. 20–22.

[30] Hsu J.S., Reber D., Method for effective color change in extrusion blow molding accumulator heads, in: Harris R.M. (Ed.), Color. Technol. Plast., William Andrew Publishing, 1999, pp. 157–161, doi:10.1016/B978-188420778-5.50020-6.

[31] Duty C., Ajinjeru C., Kishore V., Compton B., Hmeidat N., Chen X., Liu P., Hassen A.A., Lindahl J., Kunc V., What makes a material printable? A viscoelastic model for extrusion-based 3D printing of polymers, J. Manuf. Process. 35 (2018) 526–537, doi:10.1016/j.jmapro.2018.08.008.

[32] Dorgan J.R., Rheology of poly(lactic acid), Polymers (2010) 125–139, doi:10.1002/9780470649848.ch10.

[33] Osswald T.A., Menges G., Osswald T.A., Menges G., Rheology of polymer melts, Mater. Sci. Polym. Eng. (2012) 111–159, doi:10.3139/9781569905241.005.

[34] Barnes H.A., Hutton J.F., Walters K., An Introduction to Rheology, Elsevier, 1989.

[35] Gilbert M., Relation of structure to thermal and mechanical properties, Brydson's Plast. Mater., Butterworth-Heinemann, 2017, pp. 59–73, doi:10.1016/B978-0-323-35824-8.00004-9.

[36] Lim L.-T., Cink K., Vanyo T., Processing of poly(lactic acid), Polymers (2010) 189–215, doi:10.1002/9780470649848.ch14.

[37] Kister G., Cassanas G., Vert M., Morphology of poly(glycolic acid) by IR and Raman spectroscopies, Spectrochim. Acta Part A Mol. Biomol. Spectrosc. 53 (1997) 1399–1403, doi:10.1016/S0584-8539(97)00039-1.

[38] Yuniarto K., Purwanto Y.A., Purwanto S., Welt B.A., Purwadaria H.K., Sunarti T.C., Infrared and Raman studies on polylactide acid and polyethylene glycol-400 blend, AIP Conf. Proc. 1725 (2016) 020101.1-020101.6 020101.

[39] Domingos M., Chiellini F., Gloria A., Ambrosio L., Bartolo P., Chiellini E., Effect of process parameters on the morphological and mechanical properties of 3D Bioextruded poly(ε-caprolactone) scaffolds, Rapid Prototyp. J. 18 (2012) 56–67, doi:10.1108/13552541211193502.

[40]

Baptista R., Guedes M., Fatigue behavior of different geometry scaffolds for bone replacement, Procedia Struct. Integr. 17 (2019) 539–546, doi:10.1016/j.prostr.2019.08.072.

[41] Moroni L., De Wijn J.R., Van Blitterswijk C.A., 3D Fiber-Deposited Scaffolds for Tissue Engineering : Influence of Pores Geometry and Architecture on Dynamic Mechanical Properties, vol. 27, 2006, pp. 974–985, doi:10.1016/j.biomaterials.2005.07.023.

[42] Serra T., Planell J.A., Navarro M., High-resolution PLA-based composite scaffolds via 3-D printing technology, Acta Biomater. 9 (2013) 5521–5530, doi:10.1016/j.actbio.2012.10.041.

[43] Tuan S., Hutmacher D.W., A comparison of micro CT with other techniques used in the characterization of scaffolds 27 (2006) 1362–1376, doi:10.1016/j.biomaterials.2005.08.035.

[44] Szojka A., Lalh K., Andrews S.H.J., Jomha N.M., Osswald M., Bioprinting Biomimetic 3D printed sca ff olds for meniscus tissue engineering, Bioprinting 8 (2017) 1–7, doi:10.1016/j.bprint.2017.08.001.

[45] Sobinani P., Nolan D.R., Lally C., Kelly D.J., Integrating finite element modelling and 3D

Highlights

- 3D printing process parameters strongly influence scaffold mechanical properties.
- Parameters should be set after thermal and rheologic material analysis.
- Scaffold filament offset distance enabled both porosity and mechanical behavior tailoring.
- Both align and staggered scaffold configurations allows for fully interconnected pore structures.
- Staggered scaffold configurations have reduced mechanical properties due to filament bending.

Appendix A Supplementary data

The following is the Supplementary data to this article:

Multimedia Component 1

Multimedia component 1

alt-text: Multimedia component 1

Queries and Answers

Query: Your article is registered as a regular item and is being processed for inclusion in a regular issue of the journal. If this is NOT correct and your article belongs to a Special Issue/Collection please contact

p.marudhu@elsevier.com immediately prior to returning your corrections.

Answer: Yes

Query: Please confirm that given names and surnames have been identified correctly and are presented in the desired order and please carefully verify the spelling of all authors' names.

Answer: Yes

Query: Please confirm that the provided email “ricardo.baptista@estsetubal.ips.pt” is the correct address for official communication, else provide an alternate e-mail address to replace the existing one, because private e-mail addresses should not be used in articles as the address for communication.

Answer: Yes, the email is correct.

Query: Have we correctly interpreted the following funding source(s) you cited in your article: FCT; CeFEMA; Strategic Project Pest; CERENA Strategic Project?

Answer: Yes